Correlating the Chemical Composition and Size of Various Metal Oxide Substrates with the Catalytic Activity and Stability of As-Deposited Pt Nanoparticles for the Methanol Oxidation Reaction

Journal:	*Catalysis Science & Technology*
Manuscript ID	CY-ART-08-2015-001444.R1
Article Type:	Paper
Date Submitted by the Author:	05-Oct-2015
Complete List of Authors:	Scofield, Megan; Stony Brook University, Christopher, Koenigsmann; Chemistry, Bobb-Semple, Dara; Stony Brook University, Tao, Jing; Brookhaven National Laboratory, Center for Functional Nanomaterials Tong, Xiao; Brookhaven National Laboratory, Center for functional Nanomaterials Wang, Lei; SUNY Stony Brook, Lewis, Crystal; Chemistry, Vukmirovic, Miomir; Brookhaven National Laboratory, Zhu, Yimei; Brookhaven National Laboratory, Adzic, Radoslav; Brookhaven National Laboratory, Wong, Stanislaus S; SUNY Stony Brook,

SCHOLARONE™
Manuscripts

Correlating the Chemical Composition and Size of Various Metal Oxide Substrates with the Catalytic Activity and Stability of As-Deposited Pt Nanoparticles for the Methanol Oxidation Reaction

Megan E. Scofield,[1] Christopher Koenigsmann,[1] Dara Bobb-Semple,[1] Jing Tao,[2] Xiao Tong,[3] Lei Wang,[1] Crystal S. Lewis,[1] Miomir Vukmirovic,[4] Yimei Zhu,[2] Radoslav R. Adzic,[4] and Stanislaus S. Wong[1,2,*]

*To whom correspondence should be addressed.

Email: stanislaus.wong@stonybrook.edu; sswong@bnl.gov

[1]Department of Chemistry, State University of New York at Stony Brook, Stony Brook, NY 11794-3400

[2]Condensed Matter Physics and Materials Sciences Department, Building 480, Brookhaven National Laboratory, Upton, NY 11973

[3]Center for Functional Nanomaterials. Building 735, Brookhaven National Laboratory, Upton, NY

[4]Chemistry Department, Building 555, Brookhaven National Laboratory, Upton, NY 11973

Abstract

The performance of electrode materials in conventional direct alcohol fuel cells (DAFC) is constrained by (i) the low activity of the catalyst materials relative to their overall cost, (ii) the poisoning of the active sites due to the presence of carbon monoxide produced during small molecule oxidation, and (iii) the lack of catalytic stability and durability on the underlying commercial carbon support. Therefore, as a viable alternative, we have synthesized various metal oxide and perovskite materials of different sizes and chemical compositions as supports for Pt nanoparticles (NPs). Our results including unique mechanistic studies demonstrate that the $SrRuO_3$ substrate with immobilized Pt NPs at its surface evinces the best methanol oxidation performance as compared with all of the other substrate materials tested, including commercial carbon itself. Additionally, data from electron energy loss spectroscopy (EELS) and X-ray photoelectron spectroscopy (XPS) confirmed the presence of electron transfer from bound Pt NPs to surface Ru species within the $SrRuO_3$ substrate itself, thereby suggesting that favorable metal-support interactions are responsible for the increased MOR activity of Pt species with respect to the underlying $SrRuO_3$ composite catalyst material.

Short Statement of Significance:

In this manuscript, we probe alternative support materials to conventional carbon which may not only prevent aggregation and dissolution of the catalyst particles but also contribute to increased methanol oxidation activity. In this light, we have synthesized various metal oxide and perovskite support materials in order to evaluate their (i) methanol oxidation activity as catalyst materials, (ii) methanol oxidation activity as supports for Pt nanoparticles, and (iii) stability with Pt nanoparticles attached. Moreover, we have also demonstrated a plausible origin of the observed enhancement in methanol oxidation activity for our best support materials via data from electron energy loss spectroscopy and X-ray photoelectron spectroscopy. Furthermore, this manuscript fits within the scope of the journal in addressing a significant problem associated with the instability of catalyst materials when supported onto carbon for direct alcohol fuel cells.

1. Introduction

Significant strides have been made in terms of advancing direct alcohol fuel cell (DAFC) technology. However, a number of pervasive and potentially deleterious issues can significantly impact upon the overall fuel cell design and specifically reduce electrochemical performance. In particular, the nature of the electrode materials used raises an important and unavoidable concern. In particular, the (i) low activity of the catalyst materials relative to their overall cost, (ii) the poisoning of the active sites due to the presence of carbon monoxide produced during small molecule (methanol, ethanol, and formic acid) oxidation, and (iii) the lack of catalytic stability and durability on the underlying commercial carbon support all represent key inhibitors of catalytic activity and contribute to the operational degradation of electrocatalysts employed, thereby reducing the efficiency of the fuel cell as a whole.[1-3]

Currently, platinum (Pt)-containing electrocatalysts (such as alloy, core-shell, and hierarchical motifs) are the most widely utilized catalysts, due to the inherently high activity achieved by Pt, which is the most active metal for both the methanol oxidation reaction (MOR) and oxygen reduction reaction (ORR). Nevertheless, the use of carbon as the support medium not only can lead to Pt agglomeration but also is intrinsically problematic, since carbon is easily corroded over time. The net consequence is an overall loss of active Pt sites (i.e. a decrease in the active electrochemical surface area (ECSA)) and hence, the concomitant degradation of the catalyst.[1] Typically, with the use of carbon black, i.e. the most common carbon support, aggregation and detachment of previously immobilized Pt nanoparticles (NP) tend to occur. As a result, the overall surface area needed for the oxygen reduction and methanol oxidation reactions is reduced, and the observed fuel efficiency is effectively lowered.

In order to address this issue and to discover high-performing, relatively inexpensive alternatives to carbon black, research has turned to other supports such as either graphene, carbon nanotubes (CNTs), or metal oxides in order to (i) improve upon favorable physico-chemical coupling interactions of the underlying support with the catalyst and to (ii) enhance the stability of the support under highly acidic electrochemical conditions. Specifically, other groups have previously demonstrated that certain metal oxides such as TiO_2,[4-6] RuO_2,[7-9] and SnO_2[10-12] represent viable and practical alternatives to standard carbon black, due to their (a) increased chemical and electrochemical stability, (b) positive interactions with the coated electrocatalysts,[13] as well as (c) capacity to give rise to an external, outer surface composed of pendant, accessible hydroxyl groups which can conceivably facilitate the removal of poisonous, de-activating species, such as CO.[14] The ability of these metal oxides to adsorb hydroxyl groups is highly advantageous; specifically, these metal oxides possess certain geometrical configurations of metal oxide (M-O) bonds, such that when placed in water, the M-O bonds will interact and form layers of molecular water adsorbates.

Additionally, by either adding in oxygen vacancies or doping with ions such as fluorine, it is likely that these metal oxides can be tailored so as to exhibit even higher electrochemical activities.[13] Although TiO_2 and $SrTiO_3$ are known to be semiconductors in bulk, by contrast, at the nanoscale, a significant amount of defects tend to form within these materials, and these imperfections ultimately enhance their intrinsic conductivities.[15-17] For example, it has been shown that nanoscale TiO_2 possesses Ti^{3+} ions which contribute to an increase in their conductivity, and these cations are typically generated by either creating oxygen deficiencies or heating TiO_2 within a reducing atmosphere. These scenarios are analogous to the net effects of

our own experimental protocol herein, in which we have fabricated nanoscale TiO_2 by means of hydrothermal synthesis.[15-17]

Indeed, these binary metal oxides have been noted to be particularly advantageous for their corrosion resistance and electrochemical stability under highly acidic conditions, due to their intrinsically high oxidation state, because it is very difficult to oxidize these metal oxides even further. Additionally, metal oxides can act either as co-catalysts or as supports that give rise to beneficial metal-support interactions with their overlying metal catalysts.[15, 18] Typically, metal support interactions are characterized by either partial charge transfer between the support itself and the supported metal catalyst or a change in the lattice parameter of the metal catalyst.[19, 20] This important and helpful interaction can be essentially ascribed to an electronic effect created by the specific metallic component within the support, and has been previously noted with metal oxide supports such as but not limited to TiO_2, CeO_2, MoO_2, WO_2, SnO_2, and RuO_2.[15, 18-21]

To take this concept one step further, it is reasonable and appropriate to consider using either complex metal oxides or perovskites such as ABO_3 (A = Sr, La, and Ca; B = Ti and Ru) as viable metal oxide support materials. In fact, it is well documented that a variety of perovskite materials are electronically conductive, possess very good proton transport properties, and maintain acidic outer surfaces, thereby rendering them as excellent candidates for support materials in highly acidic environments, typically utilized by conventional fuel cells.[22] As a relevant and illustrative example in this context, our group has previously shown[23] that $SrRuO_3$ yields a promising level of methanol oxidation activity, even in the absence of Pt metal as a dispersed catalyst. This result provides for compelling evidence for the ability of the support material itself to actively participate in the oxidation process of methanol.

Moreover, a different team investigated the corresponding methanol oxidation behavior of $Pt/SrRuO_3$, and demonstrated its significant MOR potential.[22] That is, the use of a complex metal oxide material as a support for Pt has been shown to not only lower the overpotential for methanol oxidation but also contribute to the complete oxidation of any methanol present.[14, 24] More importantly, in the presence of water, the perovskite material appears to have the capability to readily absorb surface oxygen atoms that are likely to be heavily protonated on its surface, thereby generating hydroxyl groups which can facilitate and hence promote the desired oxidation process.[25] Some groups have proposed that the metal located at the B site, as opposed to the A site, more significantly influences and contributes to the observed electrochemical abilities of the electrocatalyst lying on its surface.[14]

Specifically, a combinatorial study by Mukasyan et al.[22] evaluated a variety of ABO_3 perovskite structures, with 'A' = La, Sr, and 'B' = Fe, Ru, for instance. In terms of results, they not only found that $SrRuO_3$ as a support is highly active towards methanol oxidation but also, after Pt nanoparticle (NP) deposition, noted that the Pt likely existed in a higher oxidative state, with the implication that the perovskite material most probably accepted electrons from the adjacent elemental Pt, thereby contributing to a higher observed MOR activity for the overall catalyst. Multiple groups have attempted to determine and differentiate the exact 'catalytic roles' of the atoms localized at both the 'A' and 'B' sites within the perovskite structure, respectively. In particular, Sauvet et al. showed that the Sr present at the 'A' site stabilizes the Ru in its tetravalent configuration at the 'B' site.[26] Additionally, Ponce and co-workers[27] highlighted a similar finding in which the Sr within the perovskite $La_{1-x}Sr_xMnO_3$ ('x' = 0–0.5) played an important role in maintaining the Mn^{4+} state.

Hence, with the ongoing need to find more stable and potentially more active alternatives as compared with conventional carbon black, perovskite materials represent a viable, attractive, and relatively little used substitute for catalytic supports. Moreover, there have been few if any systematic efforts to correlate the chemical composition of these perovskites with the resulting electrochemical performance observed. In this light, the significance of this manuscript is as follows. We aim to differentiate between the various enhancements observed at the catalytic interface as a result of the identity of 'B' site within the perovskite structure. That is, by systematically studying various perovskites wherein we have purposely altered 'B' but kept 'A' constant, we intend to determine whether the metal residing at the 'B' site is indeed the driving factor for the observed, enhanced MOR activity. Additionally, we strive to demonstrate the origin of catalytic enhancement, thereby providing a plausible rationale for explaining the improved MOR activity noted.

We have also tested for the effect of surface area and size by analyzing metal oxides of various constituent crystallite sizes. Moreover, we compare our data to binary oxide control samples to deduce between and thereby potentially explain the relevant electrocatalytic performances of simple binary versus ternary (in this case, perovskite) metal oxides. Our results demonstrate that (i) the $SrRuO_3$ substrate coated with Pt NPs gives rise to the best MOR performance observed as compared with the other substrate materials tested herein and that (ii) size is a relatively less important determinant of electrochemical activity as compared with the overriding importance of the chemical composition of the substrate materials themselves.

Furthermore, in order to probe the origin of this enhancement, electron energy loss spectroscopy (EELS) provided evidence for electron transfer from Pt NPs lying at the surface to surface Ru atoms within the underlying $SrRuO_3$ substrate itself. Interestingly, little if any

electron transfer was detected for either the TiO_2 and RuO_2 controls or even analogous $SrTiO_3$ substrates. As additional complementary corroboration of these EELS data, X-ray photoelectron spectroscopy (XPS) data were acquired and confirmed a decrease in the electron density in the Pt *4f* region when Pt NPs were deposited onto the $SrRuO_3$ supports. These cumulative results would imply that favorable metal support interactions, involving electron transfer between immobilized Pt and the underlying $SrRuO_3$, likely account for the increased MOR activity of the composite catalyst material. Moreover, based on the collected chronoamperometry data, the use of $SrRuO_3$ would also be beneficial in terms of improving the overall stability and long-term effectiveness of the catalytic support as compared with standard commercial carbon black.

2. Materials and Methods

2.1. Synthesis of metal oxide supports

2.1.1. TiO_2 Nanoparticles (11.4 nm in average diameter)

TiO$_2$ nanoparticles have been synthesized via a two-step hydrothermal protocol.[28] In particular, 0.5217 g of commercial anatase TiO_2 (Sigma Aldrich, 99.8% metals basis) is immersed in an aqueous solution of 94 mL of sodium hydroxide (NaOH) (EMD, 10 M) in water in a 120 mL autoclave, and stirred until it is homogeneous. The autoclave is then heated to 120°C and left for 24 h. After the 24 h reaction, the resulting mixture was transferred to a centrifuge tube, sonicated with water, and ultimately centrifuged. The supernatant was subsequently removed from the bottom of the tube, prior to isolation of a fine titanate powder, after additional washing steps with HCl (EMD, ACS Grade) to remove residual NaOH.

To convert the hydrogen titanate nanostructures into the corresponding TiO_2 particles, 0.05 g of the hydrogen titanate was added to 16 mL of H_2O in a 23 mL autoclave and heated to 170°C for 24 h. The resulting material was washed with H_2O to remove any excess acid.

2.1.2. RuO_2 Nanoparticles (35.0 nm in average diameter)

RuO_2 nanoparticles[29] have been fabricated as follows: 0.42 g of $RuCl_3 \cdot X\ H_2O$ (Acros Organics, 35-40% Ru) was added to 3.5 mL ethanol (Alfa Aesar, anhydrous, denatured, HPLC grade) to create a 1.5 mM solution, which was stirred vigorously until completely dissolved. Subsequently, 1.2 mL of propylene oxide (Fisher Scientific) was added as the gelation agent, and the mixture was continuously stirred until a gel was created. Once the gel was formed, the mixture was covered at room temperature and allowed to sit for 24 h. The material was then calcined in a tube furnace at 600°C for 2 h with a ramp rate of 10°C/min. After cooling, the resulting mixture was treated with H_2O_2 (Fisher Scientific, 50% stabilized, certified) in order to oxidize any Ru metal, still remaining.

2.1.3. $SrTiO_3$ Nanoparticles (40.7 nm in average diameter)

$SrTiO_3$ particles[30] were synthesized by employing a hydrothermal method. Specifically, TiO_2 (Sigma Aldrich, 99.8% metals basis, 0.18 g, 2.3 mmol) was mixed in a 20 mL aqueous solution of KOH (~45% purity for HPLC, Fluka, 1.26 g, 23 mmol) and $Sr(OH)_2 \cdot 8\ H_2O$ (Alfa Aesar, 99% metal basis, 0.508 g, 2.3 mmol) within a 23 mL autoclave. This mixture was heated to 150°C for 3 days. The autoclave was later cooled to room temperature. The resulting white powder was subsequently washed with water and then air dried overnight.

2.1.4. $SrRuO_3$ Nanoparticles (37.3 nm in average diameter)

In a typical synthesis of 40 nm diameter $SrRuO_3$ nanoparticles,[31] 0.1 g of both $RuCl_3 \cdot XH_2O$ (Acros Organics, 35-40% Ru) and strontium acetate $(Sr(CH_3COO)_2)$ (Alfa Aesar) were added to 20 mL H_2O, and stirred for 10 minutes, until the mixture was rendered homogeneous.

KOH (Fluka, ~45%, for HPLC) was added in until the pH attained a value of 13, and the solution was subsequently stirred for 1 h. The mixture was then removed from stirring, and left to stand at room temperature for 3 h. Afterwards, the material was washed with H_2O for three times, filtered, and dried overnight at 80°C. The material was ground with a mortar and pestle, and calcined at 600°C for 5 h.

2.1.5. SrRuO$_3$ Nanoparticles (146.0 nm in average diameter)

Larger SrRuO$_3$ nanoparticles[23] were prepared by combining and mixing strontium hydroxide ($Sr(OH)_2 \cdot 8H_2O$ (Alfa Aesar, 99% metal basis)), RuO_2 nanoparticles (prepared from Section 2.1.2), NaCl / KCl (1: 1) (Merck, bulk; Mallinckrodt, Baker), and 1% mineral oil (Acros Organics, pure) in Triton X-100 (EM Industries) with an effective mole ratio of 1: 1: 20: 3 using a mortar and pestle. The mixture was subsequently ground for 25 min prior to transfer to a crucible. The material was then heated to 700°C at a ramp rate of 5°C/min with a continuous flow of air, and later quenched by immediate removal from the furnace. The product was washed twice with distilled water, centrifuged, and dried overnight.

2.1.6. SrTiO$_3$ Nanoparticles (113.0 nm in average diameter)

In a typical synthesis,[32] strontium oxalate, anatase TiO_2 (Sigma Aldrich, 99.8% metals basis), NaCl (Merck, bulk), and NP-9 (Sigma Aldrich) in an effective molar ratio of 1: 1: 20: 3 were mixed and subsequently ground with a mortar and pestle for 25 min. The mixture was then transferred to a crucible and placed in a tube furnace for 3.5 h at 850°C with a ramp rate of 10°/min. The material was subsequently cooled to room temperature, washed with de-ionized water for several times, and later dried overnight.

2.2. Pt deposition on our various metal oxide substrates

Platinum nanoparticles[33, 34] were synthesized and deposited in situ on the substrates we have focused on, herein, by the following route. Specifically, a combination of

hexachloroplatinic acid hydrate ($H_2PtCl_6 \cdot 6\ H_2O$, Alfa Aesar, 99.9%, an experimentally determined optimal mass loading of 50%) and the individual metal oxide substrate being tested was placed in 5 mL H_2O and sonicated for 30 min. Subsequently, an aqueous solution of 0.1 g sodium borohydride ($NaBH_4$, Alfa Aesar, 98% powder) was added, and the mixture was further sonicated for an extra 15 min. The resulting solution was washed with distilled water and ethanol for several more times, centrifuged, and ultimately dispersed in ethanol as an ink (2 mg of catalyst / mL of ethanol).

2.3. Structural Characterization

Powder diffraction samples were prepared by drying either the relevant metal oxide support or the various catalyst samples. Powder diffractograms of as-prepared NWs were obtained on a Scintag diffractometer, operating in the Bragg-Brentano configuration with Cu Kα radiation ($\lambda = 1.54$ Å). Diffraction patterns were collected from 2θ values of either 20° or 30° to 80° at a scanning rate of 1° per minute.

In order to obtain information about the structure, morphology, size, and crystallinity of as-prepared TiO_2, RuO_2, $SrTiO_3$, and $SrRuO_3$ samples as well as of Pt-deposited counterparts, we analyzed samples using (i) scanning electron microscopy (SEM) with an analytical JEOL 7600F thermal field effect SEM (FE-SEM), operating at an accelerating voltage of 5 kV, and (ii) transmission electron microscopy (TEM) using a Technai12 BioTwinG2 TEM instrument, equipped with an AMT XR-60 CCD camera system. High resolution transmission electron microscopy (HRTEM) and selected area electron diffraction (SAED) patterns were separately acquired on a JEOL 3000F microscope, equipped with a field-emission gun operating at an accelerating voltage of 300 kV.

For XPS analysis, the solid samples were prepared by dispersing the powder samples in ethanol and subsequently drop-casting them onto a Si wafer. They were then analyzed within the vacuum chamber of a SPECS XPS system incorporating a Phoibos 100 electron energy analyzer. The chamber was evacuated to a base pressure of about $2 \cdot 10^{-10}$ torr. XPS spectra were first collected using a model XR50 Al Kα X-ray source (hν = 1486.6 eV). The reported spectra have been referenced to the C 1s peak located at 285.0 eV.[35]

The electron energy loss experiment was carried out with a double Cs-corrected JEOL JEM-ARM200F transmission electron microscope (TEM). The electron energy-loss spectra (EELS) were obtained using the scanning probe module as part of the dual EELS data acquisition mode, so that the absolute energy loss value could be efficiently calibrated. The Gatan Digital Micrograph software package was used for routine analysis of the spectra. More than ten EELS spectra were obtained from each individual sample, and representative results are highlighted in the Figures.

2.4. Electrochemical Characterization

Electrochemical characterization of both of our metal oxide supports and Pt-deposited counterparts was performed with the catalysts supported onto a glassy carbon electrode (GCE; 5 mm, Pine Instruments). Initially, the electrode was polished using an aluminum oxide powder slurry (i.e. 0.050 μm particle size). The catalysts were subsequently dispersed in ethanol (at a concentration of 2 mg/mL) and loaded onto a modified GCE by adding two drops (i.e. 5 μL per drop) of the catalyst dispersion onto the surface, which was subsequently allowed to air dry. The GCE was later sealed with one 5 μL drop of an ethanolic 0.025% Nafion solution, prepared from a 5% stock solution.

Prior to electrochemical analysis, the catalyst-loaded GCE was immersed into fresh aliquots of water, so as to remove any impurities. In order to prepare the commercial standard, Pt NPs possessing a 20% precious metal content (ETek) were rendered into catalyst ink dispersions (1 mg/mL) in 25% isopropyl alcohol in water and deposited directly onto the surface of a polished GCE for characterization. Electrochemical measurements were obtained in 0.1 M sulfuric acid (Fisher Scientific, optima grade) solutions, created using high-purity water possessing a resistivity value of 18.2 MΩ•cm. Pt foil and an Ag/AgCl combination (3 M Cl$^-$) served as the counter and reference electrodes, respectively. All potentials have been reported with respect to the reversible hydrogen electrode (RHE).

The corresponding electrochemical properties of the catalysts were examined by cyclic voltammetry (CV). CVs were obtained in the desired argon-saturated electrolyte at a scan rate of 20 mV/s. The active electrochemically accessible surface area (ECSA) was calculated from the integrated hydrogen adsorption (H_{ads}) determined in the cyclic voltammetry analysis, utilizing 210 $\mu C/cm^2$ as the conversion factor. As-obtained ECSA values represent a reasonable estimate of the active Pt sites in the system.

2.5. Measurement of MOR Kinetics

The MOR kinetics were measured by first obtaining CVs at a scan rate of 20 mV/s using a de-oxygenated 0.5 M methanol (Fisher Scientific, Optima grade) solution, supported in a 0.1 M H_2SO_4 electrolyte. Typically, a linear-sweep voltammogram (LSV) was obtained in the anodic sweep direction, so as to collect additional MOR kinetics curves. The observed current was subsequently normalized to the Pt surface area, which can be determined from the H_{ads} charge. After the initial LSV, we obtained additional MOR CVs so as to ensure that the surface of the

catalyst was sufficiently stable in order to generate more reproducible CVs. Tafel plots were generated from MOR CVs, collected at a scan rate of 1 mV/s.

Chronoamperometry (CA) was also run in order to test the stability of our as-prepared catalysts. Specifically, chronoamperograms were acquired in a de-oxygenated 0.5 M methanol solution, supported in a 0.1 M H_2SO_4 electrolyte. The electrode was submerged and tested, while the potential was maintained at a value of 0.7 V for a period of one hour. This specific potential was chosen, due to the fact that it designates a potential value which resides within the peak current region of all of the catalysts tested herein, thereby allowing for an appropriate comparison of relative activity amongst all samples analyzed. In particular, the activity of our novel catalysts has been compared with respect to that of Pt NP/C (Etek), which had served as a commercial standard and control.

3. Results & Discussion

In this manuscript, we seek to investigate the impact of the chemical composition of the support material itself upon the overall activity of the catalyst. That is, we address the issue of how specifically varying the identity of the 'B' metal site within a perovskite material ultimately promotes and enhances the oxidation of methanol. As a constant 'parameter', Sr was chosen for the invariant 'A' site, since it has been shown to be electrochemically passive.[36] In probing the effect of Ru in particular as the 'B' site, titanium was utilized as a corresponding 'counterbalancing' element, since Ti itself possesses neither a promotional effect nor sufficient conductivity.[37] It has been previously documented that altering the nature of the substituents at the 'B' site can significantly contribute to electrochemical activity.[14, 24] Specifically herein, we demonstrate not only a reproducible electrochemical enhancement when Ru is localized as the

'B' site but also the underlying nature of this enhancement by utilizing EELS analysis. In so

doing, we demonstrate electron transfer between Pt and Ru within the $SrRuO_3$ substrate, which

may plausibly account for the improved MOR performance. Moreover, in addition to

commercial Pt/C, both TiO_2 and RuO_2 served as further controls for these perovskite supports.

The structure, morphology, purity, and crystallinity of our perovskite materials both before and

after Pt deposition were analyzed using a suite of complementary structural characterization

techniques, including XRD, SEM, HRTEM, SAED, XPS, and EELS.

3.1. Characterization of the Various Metal Oxide and Perovskite Support Materials

Specifically, Figure S1 depicts the powder XRD of various perovskite materials tested,

including not only of both sizes of $SrTiO_3$ and $SrRuO_3$ but also of the TiO_2 and RuO_2 control

samples. All six metal oxide samples gave rise to the expected crystallographic structure, as

demonstrated by the JCPDS database standard of each material. In particular, Figure S1A is

associated with the anatase form of TiO_2, with peaks corresponding to JCPDS 21-1272. Figure

S1B can be ascribed to the tetragonal structure of RuO_2, with the peak values and locations

consistent with JCPDS 73-1469. Additionally, the $SrTiO_3$ samples (Figure S1C & S1E) evince a

cubic structure similar to JCPDS 86-0179, whereas the $SrRuO_3$ samples (Figure S1D & S1F)

could be readily identified with an orthorhombic structure (JCPDS 85-1907). Moreover, all metal

oxide samples displayed the correct structure with little if any obvious impurities, as had been

expected, based on the original synthesis protocols.[23, 28-32]

The morphological and chemical compositional characterization data for the various

metal oxide and perovskite materials tested are highlighted in Figures 1 and 2, respectively.

These include results obtained from scanning electron microscopy (SEM), transmission electron

microscopy (TEM), high-resolution TEM (HRTEM), as well as selected area electron diffraction

(SAED) analysis. Specific data associated with the average diameters, measured d-spacings, and particular crystallographic planes of our binary and ternary metal oxides are listed in Table 1.

Relevant, representative data on the morphology as well as the chemical composition of (i) our TiO_2 and RuO_2 nanoparticles in addition to (ii) our as-synthesized perovskite metal oxide nanoparticles can be found in Figures 1 and 2, respectively, as well as in the Supplementary Information (SI) section. As mentioned earlier, our TiO_2 NPs were fabricated hydrothermally, our RuO_2 NPs were generated by utilizing a sol-gel protocol, and lastly, our perovskite nanostructures were produced using both molten salt techniques as well as hydrothermal methods. Nonetheless, in spite of the variation in synthesis technique, all of our collected data are definitely consistent with the prior results in terms of morphology, degree of monodispersity and homogeneity, crystallinity, as well as chemical composition for these various systems.

The Brunaeur-Emmett-Teller (BET) analyses for each of the binary metal oxide and ternary complex metal oxide materials along with their respective sizes are presented in Table 1. The results obtained from BET characterization are particularly significant for understanding the role and functionality of supports, since materials possessing small surface areas tend to be more prone to potentially deleterious catalyst sintering and Ostwald ripening effects. These mechanisms are responsible for the aggregation of Pt, and can thereby reduce the electrochemically active surface area (ECSA) of the tested material, thereby ultimately decreasing the number of available sites for methanol oxidation. The measured surface areas were found to increase in the following order: 35 nm RuO_2 < 146 nm $SrRuO_3$ < 113 nm $SrTiO_3$ < 40.7 nm $SrTiO_3$ < 37.3 nm $SrRuO_3$ < 11.4 nm TiO_2. All BET values were found to be consistent with other measured BET data for each metal oxide tested herein, possessing a particular range in size, as noted from prior literature.[14, 23, 38-42] It is also important to note that the synthesis

method plays an important role in controlling the overall surface area of the material. A table

including data from metal oxides synthesized by others with similar BET surface area analysis

measurements to our own can be found in the SI, which support our own BET data (Table S1).

3.2. Characterization of our Various Metal Oxide and Perovskite Metal Oxide Support

Materials after Pt Deposition

The deposition of Pt nanoparticles (NP) onto the various metal oxide and perovskite

supports was initiated using a $NaBH_4$ reduction method. Therefore, in order to evaluate the

optimal Pt loading for methanol oxidation in an H_2SO_4 electrolyte, a systematic series of Pt NPs

immobilized onto a TiO_2 support (used as a control) with various mass loadings was tested. As

others have previously noted, an optimal Pt mass loading of 50% generated the highest level of

MOR activity discerned, with no significant additional increase after 50% loading.[37] Therefore,

with the need to utilize the least amount of Pt possible without impacting upon the observed

performance, a 50% Pt mass loading was used for each electrocatalyst sample tested.

Additionally, based upon the HRTEM results highlighted in Figure 3 (which will be described in

more detail below), a generally uniform spatial distribution of NPs evenly dispersed onto the

underlying metal oxide surface was observed.

High-resolution TEM images of the various metal oxide samples prepared after Pt

deposition are shown in Figure 3. The Pt NPs possess a rather uniform average particle diameter,

ranging from 2-4 nm, for each and every sample analyzed with a relatively homogeneous

distribution, as mentioned above. The *d*-spacings corresponding to both the Pt and the metal

oxide support for each material, respectively, have been indexed. Table 2 incorporates data on

the various measured *d*-spacings and the corresponding planes for both the metal oxide substrate

as well as the overlying Pt NPs. Overall, all of the measured *d*-spacings can be assigned to the

expected crystallographic structures for each of the samples, with the Pt (111) facet noted as the

most predominantly exposed facet observed for the adsorbed particles. It should also be

mentioned that for both of the analyzed samples incorporating $SrRuO_3$ supports, we observed a

~2% increase in the *d*-spacings of the immobilized Pt NPs. Although these values fall within the

error of the measurement, these discrepancies could also be plausibly attributed to the presence

of tension strain imparted onto Pt by the presence of the underlying substrate material, thereby

resulting in an expansion of the Pt lattice, a scenario which has been previously shown to

improve methanol oxidation activity.[43] Additionally, SAED patterns possessing rings attributed

to both the metal oxides as well as to the Pt NPs present can be found in the SI (Figure S3).

3.3. Electrochemical Activity of our Metal Oxide and Perovskite Support Materials

The methanol oxidation reaction activity of the various metal oxide support materials was

probed using cyclic voltammetry in a 0.1 M H_2SO_4 solution containing 0.5 M methanol (Figure

4). The collected CVs indicate that the bare $SrTiO_3$ substrates evinced noticeably higher MOR

activities as compared with other analogous substrates, including Ru-based support materials due

to the presence of the anodic current apparent during the negative sweep. The decreased activity

of the Ru-containing substrates may be attributed in part to the increased amount of adsorbed

hydroxyl species, inhibiting the adsorption and subsequent oxidation of methanol. This assertion

is consistent with the nature of the CVs collected prior to methanol oxidation, which are

collected in Figure S2. Additionally, it is worth remarking that CVs collected on RuO_2 substrates

in sulfuric acid electrolyte have also exhibited similar peak profiles, which others have attributed

to the presence of hydroxyl groups.[44, 45] Specifically, these CVs (Figure S2) imply that the Ru-

containing substrates gives rise to apparent oxygen adsorption features, whereas there is no

evidence for oxygen adsorption in the analogous Ti-containing support data. It is worth noting

that although the SrRuO$_3$ supports do not demonstrate an improved MOR activity as compared with analogous SrTiO$_3$ substrates, the addition of Pt NPs should generate Pt-Ru pair sites that will be highly beneficial towards enhancing methanol oxidation activity.

The overall stability of each of the catalyst support materials has been evaluated and is depicted in Figure 5. Specifically, the degree of stability has been tested by cycling each material for 1000 cycles at 250 mV/s in an 0.1 M H$_2$SO$_4$ electrolyte in order to evaluate the change in available surface sites as well as in the corresponding electrochemical activity. In particular, the TiO$_2$, RuO$_2$, and SrTiO$_3$ samples evince reasonable stability over 1000 cycles, as can be concluded by the reproducible nature of the curves at cycle 1 versus cycle 999. However, an increase in activity is seen with both of the SrRuO$_3$ samples tested. In order to determine the cause for this increase, a TEM analysis of these two samples, post cycling, can be seen in Figure S4, and the SrTiO$_3$ samples analyzed measure 38.1 ± 3.9 nm and 194.8 ± 22.6 nm, respectively . Based on these images, it can be observed that the surfaces of both of these SrRuO$_3$ samples are becoming more perceptibly roughened as opposed to experiencing any appreciable change in either size or intrinsic morphology. Therefore, this apparent increase in activity for both SrRuO$_3$ samples can likely be ascribed to the formation of new Ru-O active sites that possess lower coordination numbers and are hence more catalytically active. Hence, on the basis of all of these data, our samples appear to be stable without a distinctive alteration in either size or morphology.

3.4. Electrochemical Activity of our Metal Oxide and Perovskite Support Materials after Pt Deposition

In order to assess the electrochemical activity of our materials after Pt deposition, as shown in Figure 6, CVs were collected for each material in 0.1 M H$_2$SO$_4$, in order to investigate and correlate the impact of the support materials with the overall electrochemical performance.

Regarding the substructure of the CVs, the shape and location of the observed hydrogen and oxygen adsorption features associated with the Pt/TiO_2 sample are consistent with prior reports.[46] Moreover, the $Pt/SrTiO_3$ samples evince similar attributes to those observed for Pt itself. Interestingly, the peaks in both regions can be solely attributed to the Pt NPs themselves at the surface, an observation indicative of the fact that the identity of the 'A' site metal, Sr, likely does not itself contribute significantly to the adsorption of hydroxyl groups; this assertion is supported by Figure S2 as well as by prior reports.[23] In fact, both strontium and titanium are known to be "inactive" and electrochemically passive, since they do not possess obvious active sites for adsorption.[36, 37] By contrast, the RuO_2 and $SrRuO_3$ samples maintain peaks in the hydrogen and oxygen adsorption regions, which are similar to what has been previously observed with Pt/RuO_2 materials.[9, 47]

Moreover, electron energy loss spectroscopy (EELS) was employed for the first time to probe the nature of the surface interactions between Pt and these metal oxide support materials in order to gain further insights into the corresponding electrochemical performance. To summarize, because there was little if any difference in the shape of EELS spectra associated with the various TiO_2, RuO_2, and $SrTiO_3$ samples either before or after Pt deposition (Figure S5), there was likely no apparent charge transfer in these systems that we could readily distinguish and differentiate. By contrast, both of the $SrRuO_3$ samples gave rise to a suppression of the Ru M_4 edge, in particular after Pt NP coverage, as can be observed in Figure 7.[48] This reduction in the Ru M_4 signal, associated with the Ru $4p$ orbitals, is evident and noticeable, and is likely indicative of electron acceptor behavior. This signal suppression would infer that electron transfer is occurring from Pt to Ru within the $SrRuO_3$ support material, and, as a result, there is a decrease in the number of Pt electrons available, as previously demonstrated by prior reports.[49-51]

Ultimately, this situation would not only lead to a decrease in the amount of poisonous species potentially blocking Pt active sites but also allow for increased methanol adsorption at these Pt active sites. One group[22] noted that, after Pt deposition onto a SrRuO$_3$ substrate, Pt was likely oxidized to Pt^{+2} from a neutral Pt^0 state, thereby further supporting our EELS-derived notion that the presence of an oxidized Pt species is necessary for high alcohol oxidation activity. It should be noted that the Pt^0 was not likely to have been completely oxidized to the Pt^{+4} state, since the latter species is known to be ineffective at promoting methanol oxidation.[52]

To further probe the nature of the electron transfer from Pt, XPS (Figure 8) was used to more closely examine the Pt *4f* region in order to confirm the postulated presence of electron donation from Pt to Ru. The Pt *4f* region contains two peaks, consisting of low energy band (*4f$_{7/2}$*) and high energy band (*4f$_{5/2}$*) regions. As noted in Figure 8, significant upshifts in the *4f$_{7/2}$* band energy are detected upon deposition of Pt onto both of the SrRuO$_3$ supports tested (i.e. +680 meV and +980 meV for the 146 nm SrRuO$_3$ and 37.3 nm SrRuO$_3$ supports, respectively), as compared with a control support of Pt/C itself. This upshift would indicate a loss of electron density within the Pt *4f* region.[53, 54] This result not only supports our EELS findings that electron transfer is indeed occurring from the Pt *4f* to the Ru *4p* orbitals but also corroborates the presence of a metal support interaction between the Pt NPs and the underlying SrRuO$_3$ support.

In order to evaluate the methanol oxidation ability of the materials, the linear sweep voltammograms (LSVs) are included in Figure 9A, with the full sweeps (forward and reverse) seen in Figure S6. The corresponding activities of the various materials probed at 0.55 V vs. RHE are summarized in the bar graph in Figure 9B. A complementary set of activities measured at 0.7 V vs. RHE is highlighted in Table 3. Specifically, the Pt/SrRuO$_3$ (average diameter of 37.3 nm) sample achieved the highest activity of 1.42 mA/cm^2 with the larger Pt/SrRuO$_3$ sample

(average diameter of 146 nm), possessing an activity of 0.57 mA/cm^2, with data on both systems

collected at 0.7 V vs. RHE. These measured activities are consistent with the trend in the surface

areas of the underlying support materials (Table 1). In particular, the higher the surface area, the

more uniform the dispersion of Pt, and hence, the more active sites available for methanol

oxidation. A similar trend was observed for the 2 sizes of $SrTiO_3$ samples produced with the

electrochemical data taken at a slightly higher potential (0.9 V vs. RHE). In this case, Pt/SrTiO$_3$

(average diameter of 40.4 nm) gave rise to a peak activity of 0.82 mA/cm^2, whereas the larger

sample, i.e. Pt/SrTiO$_3$ (average diameter of 113 nm), yielded a peak activity of 0.75 mA/cm^2. It

is worth pointing out that even though bare $SrTiO_3$ substrates were indeed more active for

methanol oxidation as compared with their uncoated $SrRuO_3$ analogues, the presence of Pt-Ru

pair sites created after Pt deposition significantly increased the methanol oxidation activity

observed in the presence of $SrRuO_3$. This observation further corroborates the existence of

favorable metal-support interactions, facilitated and engendered by the use of $SrRuO_3$ as the

support material, an idea which is further reinforced by the EELS/XPS confirmation of electron

transfer between the Pt catalyst and the underlying $SrRuO_3$ support material.

By analyzing the onset region of Figure 9A, it is apparent that both Pt/SrRuO$_3$ (average

diameter of 37.3 nm) and Pt/SrRuO$_3$ (average diameter of 146 nm) maintain very similar onset

potentials, i.e. 0.43 V and 0.45 V vs. RHE, respectively. A comparable proximity in onset

potentials was also observed for both Pt/SrTiO$_3$ (avg. diameter of 40.7 nm) and Pt/SrTiO$_3$ (avg.

diameter of 113 nm) samples; in fact, we measured an onset potential of 0.63 V vs. RHE for both

systems. These observations would indicate that the *chemical composition* as opposed to the size

of the support is the more significant determinant of the onset potential. As such, it is evident

that the use of the Ru-containing supports gave rise to lower onset potentials as compared with

those supports containing Ti. Hence, the improvements observed for the Ru-containing

substrates as compared with Ti-rich supports would imply that the former are more active for

methanol oxidation. Additionally, our Pt/SrRuO$_3$ samples manifested higher specific activities as

compared with other Pt/metal oxide support systems reported within the literature and

summarized in the Supporting Information (Table S2). Significantly, we emphasize that our data

were obtained in the absence of carbon additives, thereby rendering our metal oxide systems as

important, relevant, and viable alternatives to the use of conventional carbon black.

Previous studies on the use of Pt/SrRuO$_3$ towards methanol oxidation have implied that

the Ru-O surface sites likely play an important role in not only removing CO from Pt active sites

but also contributing to the efficacy of methanol oxidation, as was previously shown.[22] In

support of this hypothesis, it has been claimed that the increased localized presence of tetravalent

Ru species at the surface within La$_{0.7}$Sr$_{0.3}$Cr$_x$Ru$_{1-x}$O$_3$ can significantly contribute to the increased

oxidation of CO at Pt active sites.[55] All of these previous results would collectively suggest that

the presence of Ru is a positive driving force for increased MOR activity, while the intrinsic

perovskite structure enhances the overall stability of the support itself. Based on our results, a

slight shift in the MOR onset potential can be seen between the Pt/SrTiO$_3$ samples and the

corresponding Pt/TiO$_2$ control, an observation which would further support the notion that

perovskite materials can adsorb hydroxyl groups at their external surfaces in order to facilitate

the methanol oxidation process. However, by contrast with Ru, the Pt/TiO$_2$ and Pt/SrTiO$_3$

samples possess similar peak MOR activities, which would indicate an inability of both Sr and Ti

to contribute to the methanol oxidation itself. Previous reports[27] have postulated that the A site

within a perovskite structure may actually contribute to the stability of the B site metal as

opposed to actively participating in the methanol oxidation reaction itself, thereby further reinforcing our claims herein.

In Figure 10, we have attempted to correlate the methanol oxidation activity with the Pt ECSA values associated with the various supports. Table S3 summarizes the calculated Pt ECSA data for each support analyzed, essentially normalized for the same quantity of Pt used for each sample. Specifically, when comparing the $SrRuO_3$ (146 nm) sample, which maintains an ECSA value of 3.35 cm^2, with the analogous $SrTiO_3$ (113 nm) sample, which possesses an ECSA amount of 4.31 cm^2, a higher activity was noted with the former Ru-containing support. It can be inferred that since the Pt ECSA associated with $SrRuO_3$ is actually less than the corresponding ECSA value assigned to $SrTiO_3$, the observed enhancement in methanol oxidation activity with $SrRuO_3$ must be a result of other effects. Therefore, one plausible explanation accounting for our observations with our $Pt/SrRuO_3$ samples would be the presence of electron transfer from immobilized Pt NPs to the underlying Ru-containing support, as highlighted by the EELS and XPS analysis shown in Figures 7 and 8, respectively.

When the inherent support size is reduced to an even smaller scale, an increase in both activity as well as ECSA can be observed. Specifically, when comparing the data associated with the $SrRuO_3$ (37.3 nm) and analogous $SrTiO_3$ (40.7 nm) substrates, the corresponding ESCA values are 7.45 cm^2 and 4.81 cm^2 for $SrRuO_3$ and $SrTiO_3$, respectively. A dramatic increase in activity was noted for $SrRuO_3$, even though the two substrates are comparable in size. Yet, it is unlikely that this performance enhancement could be solely attributed to the greater Pt ECSA value for $SrRuO_3$. Rather, it is plausible that the electronic effects associated with Pt interactions with the underlying $SrRuO_3$ support might also have contributed to the observed result.

The Pt ECSA values of SrRuO$_3$ (146 nm) and SrRuO$_3$ (37.3 nm) are 3.35 and 7.45 cm^2, respectively. In this case with SrRuO$_3$, we note that there is a direct and unambiguous correlation between the measured ESCA data and the resulting electrochemical activity measured; specifically, the higher the ESCA, the better the electrochemical performance. Therefore, since similar types of electronic effects and interactions are likely present within both samples, the higher activity ascribed to the smaller 37.3 nm SrRuO$_3$ support would likely be due to its increased Pt ECSA value as compared with the corresponding value for the larger analogous support material. To summarize, our data highlight the fact that the resulting observed electrochemical activity data can be ascribed to a combination and convolution of effects attributed not only to the Pt ECSA values but also to the electronic interactions induced by the perovksite oxide support with respect to the immobilized Pt nanoparticles.

In order to evaluate the MOR mechanism responsible for the activity of our best catalyst, namely Pt/SrRuO$_3$ (37.3 nm), Tafel plots were collected at potentials between 0.4 and 0.75 V vs. RHE at a scanning rate of 1 mV s^{-1}. The data are shown in Figure 11. In effect, our high-performance system achieved a Tafel slope of 0.112 V/decade, which correlates well with the theoretical value expected of Pt (0.118 V/decade) for a one-electron transfer process.[56-58] This one-electron transfer process is considered to be the rate-determining step within this potential window, and corresponds to the splitting of the first C-H bond of the CH$_3$OH molecule. A commercial Pt/C catalyst control sample tested gave rise to a Tafel slope value of 0.142 V/decade. This value is also within range of the predicted value for platinum and is similarly suggestive of a one-electron transfer process. However, the slightly smaller value attained by our 'optimal' Pt/SrRuO$_3$ catalyst would imply a beneficially more facile methanol electro-oxidation ability as compared with commercial Pt.[57] Moreover, these data further underline our claim that a

metal-support interaction is essential and likely responsible for the improved MOR activity

detected, when $SrRuO_3$ is employed as the support material.

Chronoamperometry testing of our various Pt/metal oxide electrocatalysts is presented in

Figure 12. The test was conducted over a period of 60 minutes at (E) vs. RHE = 0.7 V, which is

located within the methanol oxidation peak current region. The dramatic initial activity loss for

all electrocatalysts can be attributed to the presence of the intermediate species CO, potentially

poisoning the Pt active sites.[59, 60] As noted, the Ru-containing support materials evinced the

highest measured activity over the 60 minute period, with the Pt/$SrRuO_3$ (average diameter of

37.3 nm) sample and the Pt/$SrRuO_3$ (average diameter of 146 nm) sample, giving rise to steady

state activities of 2.8 mA/cm^2 and 2.2 mA/cm^2, respectively. The remaining steady state activity

values can be found in Table 3. We postulate and confirm that the Ru-containing species would

be expected to possess higher steady state current densities due to the presence of Ru active sites

that can also participate in the methanol oxidation process. Although the commercial Pt/C

exhibited a higher initial activity as compared with the Ti-containing samples, this result is not

surprising, considering that Pt/C is more conductive. However, the stability of all of the oxide-

containing support materials, even those containing Ti, significantly outperforms that of

commercial analogues over time, due to the ability of these metal oxide materials to more

effectively and more consistently oxidize harmful CO species at the Pt-metal oxide interface.

4. Conclusions

In this manuscript, various metal oxide support materials have been synthesized. These

support materials were characterized using a suite of techniques in order to verify their

composition, size, morphology, structural integrity, and chemical purity as well as

electrochemical ability. Pt NPs were then deposited onto these supports to evaluate methanol

oxidation performance. In the case of ABO_3 perovskites used as supports, the effect of using Ru

and Ti as the variable 'B' site was explicitly tested, while maintaining Sr as the constant 'A' site.

The electrochemical findings indicate a significant electrochemical contribution from Ru

at the 'B' site, an observation which had previously been proposed by others[14, 24] and more

importantly, confirms prior theoretical hypotheses. In effect, the presence of Ru within the

$SrRuO_3$ perovskite structure not only contributed to a significant increase in the methanol

oxidation activity but also resulted in an overall shift to lower MOR onset potentials as compared

with both analogous $SrTiO_3$ samples and binary metal oxides, used as control samples.

Moreover, we confirmed that *chemical composition* as opposed to the size of the support is the

more significant indicator of electrochemical behavior. Furthermore, a small shift to lower MOR

onset potentials was also noted for $SrTiO_3$ as compared with TiO_2, which may indicate that Sr

also plays a small but important role in adsorbing hydroxyl species, thereby facilitating the full

oxidation process of methanol.

Additionally, energy electron loss spectroscopy has been employed in order to analyze

and interpret the degree of charge transfer happening at the surface between the Pt and the

underlying metal oxide interface. As a result, we have shown that electron transfer is occurring

between the Pt NPs and the underlying $SrRuO_3$ support, thereby leading to a decreased

adsorption of CO species and an increase in the presence of additional available Pt active sites

for methanol oxidation. Moreover, XPS demonstrated an upshift associated with the Pt *4f* region

for both $Pt/SrRuO_3$ substrates as compared with the analogous Pt/C control sample, indicative of

a decrease in the electron density connected to the Pt. In particular, our cumulative data suggest

that electron transfer from Pt to the Ru in the $SrRuO_3$ material likely occurs via a Pt *4f* to Ru *4p*

transition. In the case of Pt immobilized onto $SrRuO_3$ supports, the magnitude of the Pt ECSA value does in fact correlate with the observed methanol oxidation activity, and as such, helps to explain the higher activities attained of 1.42 mA/cm^2 (Pt/$SrRuO_3$ (average diameter of 37.3 nm)) and 0.57 mA/cm^2 (Pt/$SrRuO_3$ (average diameter of 146 nm)) at E(V) vs. RHE = 0.7 V, respectively, as compared with what has been achieved with conventional C-based systems.

Furthermore, a Tafel plot was generated in order to evaluate the methanol oxidation reaction mechanism of our most effective catalyst tested, i.e. Pt/$SrRuO_3$ (37.3 nm), as compared with commercial Pt/C. In effect, our catalyst gave rise to a measured slope value (0.112 V/decade in this case versus 0.142 V/decade for commercial Pt/C), which was numerically very close to what was theoretically expected for a one-electron transfer reaction involving Pt (i.e. 0.118 V/decade). Significantly, these data implied a more facile capability of oxidizing methanol with the use of our Pt/$SrRuO_3$ catalyst. Moreover, the combined results from our Tafel plot analysis as well as from cumulative XPS and EELS data confirm the presence of a beneficial and advantageous metal-support interaction between the Pt nanoparticles and the underlying $SrRuO_3$ support, thereby implying the viability of utilizing this specific perovskite metal oxide-based support as a practical alternative to conventional carbonaceous materials.

Figure Captions

Figure 1. Representative TEM image (A & D), higher magnification HRTEM image with the measured d-spacing (B & E), and associated single area electron diffraction data (C & F) for binary 11.4 nm TiO_2 (A-C) and 35 nm RuO_2 (D-F) NPs, respectively.

Figure 2. Representative SEM images (A, D, G, J), higher magnification HRTEM images with the measured d-spacings (B, E, H, K), as well as associated single area electron diffraction data (C, F, I, L) for 40.7 nm $SrTiO_3$ (A-C), 37.3 nm $SrRuO_3$ (D-F), 113 nm $SrTiO_3$ (G-I), and 146 nm $SrRuO_3$ (J-L) NPs, respectively.

Table 1. Table highlighting the perovskite material, the average measured diameters (nm), the Brunauer–Emmett–Teller (BET) measurements, the measured d-spacings (Å) as well as the corresponding lattice planes, in addition to the actual, expected d-spacings (Å) associated with these lattice planes.

Figure 3. Representative high-resolution TEM micrographs with measured d-spacings, corresponding to both the Pt NPs and the corresponding supports for (A) Pt/TiO_2 NPs (11.4 nm), (B) Pt/RuO_2 NPs (35 nm), (C) $Pt/SrTiO_3$ NPs (40.7 nm), (D) $Pt/SrRuO_3$ NPs (37.3 nm), (E) $Pt/SrTiO_3$ NPs (113 nm), and (F) $Pt/SrRuO_3$ NPs (146 nm), respectively.

Table 2. Table associated with Figure 3, corresponding to the measured d-spacings (Å) and lattice planes of various Pt/metal oxide species, incorporating both binary and ternary perovskite oxide materials.

Figure 4. Cyclic voltammograms associated with the methanol oxidation reaction in an argon-saturated 0.1 M H_2SO_4 + 0.5 M MeOH solution, obtained at a scan rate of 20 mV/s for (A) 11.4 nm TiO_2 NPs, (B) 35 nm RuO_2 NPs, (C) 40.7 nm $SrTiO_3$ NPs, (D) 37.3 nm $SrRuO_3$ NPs, (E) 113 nm $SrTiO_3$ NPs, and (F) 146 nm $SrRuO_3$ NPs, respectively.

Figure 5. Cyclic voltammograms obtained in an argon-saturated 0.1 M H_2SO_4 solution and collected at a scan rate of 250 mV/s for 1000 cycles (only the first and last are included) for (A) 11.4 nm TiO_2 NPs, (B) 35 nm RuO_2 NPs, (C) 40.7 nm $SrTiO_3$ NPs, (D) 37.3 nm $SrRuO_3$ NPs, (E) 113 nm $SrTiO_3$ NPs, and (F) 146 nm $SrRuO_3$ NPs, respectively.

Figure 6. Representative CV curves in an argon-saturated 0.1 M H_2SO_4 solution, obtained at a scan rate of 20 mV/s with the current normalized to ECSA for (A) Pt/TiO_2 NPs (11.4 nm), (B) Pt/RuO_2 NPs (35 nm), (C) Pt/$SrTiO_3$ NPs (40.7 nm), (D) Pt/$SrRuO_3$ NPs (37.3 nm), (E) Pt/$SrTiO_3$ NPs (113 nm), and (F) Pt/$SrRuO_3$ NPs (146 nm), respectively.

Figure 7. Electron energy loss spectra for the series of (A) $SrRuO_3$ (37.3 nm) vs. Pt/$SrRuO_3$ (37.3 nm) and for the corresponding series of (B) $SrRuO_3$ (146 nm) vs. Pt/$SrRuO_3$ (146 nm) samples, respectively. Peaks presented below 300 eV represent the Carbon *K* edge peaks associated with the underlying carbonaceous TEM grid.

Figure 8. XPS spectra associated with the Pt *4f* region for Pt/C, Pt/$SrRuO_3$ (37.3 nm), and Pt/$SrRuO_3$ (146 nm), respectively. A significant upshift is observed when Pt is deposited on both $SrRuO_3$ surfaces as compared with conventional carbon.

Figure 9. (A) Cyclic voltammograms for the methanol oxidation reaction in an argon-saturated 0.1 M H_2SO_4 + 0.5 M MeOH solution, for Pt/TiO_2 NPs (11.4 nm) (black), Pt/RuO_2 NPs (35 nm) (red), Pt/$SrTiO_3$ NPs (40.7 nm) (green), Pt/$SrRuO_3$ NPs (37.3 nm) (blue), Pt/$SrTiO_3$ NPs (113 nm) (cyan), and Pt/$SrRuO_3$ NPs (146 nm) (magenta), respectively, as compared with commercial standards (i.e. Pt NP/C) (yellow), obtained at a scan rate of 20 mV/s with the current normalized to ECSA. (B) Bar graph highlighting the MOR activity data obtained at E (V) vs. RHE = 0.55 V for Pt/TiO_2 NPs (11.4 nm) (black), Pt/RuO_2 NPs (35 nm) (red), Pt/$SrTiO_3$ NPs (40.7 nm) (green),

Pt/SrRuO$_3$ NPs (37.3 nm) (blue), Pt/SrTiO$_3$ NPs (113 nm) (cyan), and Pt/SrRuO$_3$ NPs (146 nm) (magenta), respectively, as compared with commercial standards (i.e. Pt NP/C) (yellow).

Figure 10. Methanol oxidation activity (mA/cm^2) at 0.55 V as a function of the normalized Pt electrochemically active surface area (cm^2) for the various Pt/metal oxide catalysts.

Figure 11. Tafel plot data of (A) commercial Pt/C and (B) Pt/SrRuO$_3$ (37.3 nm), collected between 0.4 – 0.75 V vs. RHE at a scanning rate of 1 mV/sec.

Figure 12. Chronoamperometry measurements of catalysts, composed of Pt/TiO$_2$ NPs (11.4 nm) (black), Pt/RuO$_2$ NPs (35 nm) (red), Pt/SrTiO$_3$ NPs (40.7 nm) (green), Pt/SrRuO$_3$ NPs (37.3 nm) (blue), Pt/SrTiO$_3$ NPs (113 nm) (cyan), and Pt/SrRuO$_3$ NPs (146 nm) (magenta), respectively, as compared with commercial standards (i.e. Pt NP/C) (yellow) in an argon-saturated 0.1 H$_2$SO$_4$ + 0.5 M CH$_3$OH solution, obtained at a potential of 0.7 V vs. RHE for a test period of 60 min.

Table 3. Table consisting of measured MOR activities (mA/cm^2) and steady state current densities (mA/cm^2), obtained after 60 minutes, for various series of catalyst materials.
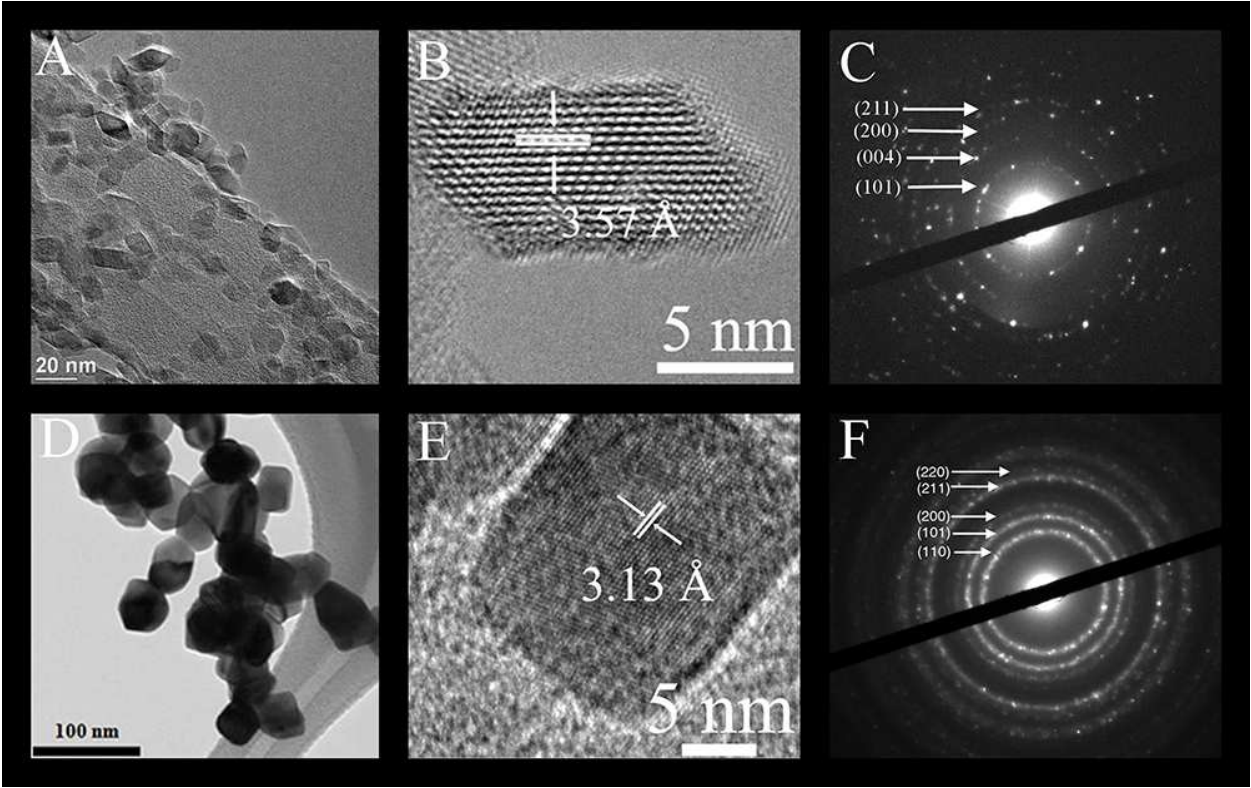
Figure 1.
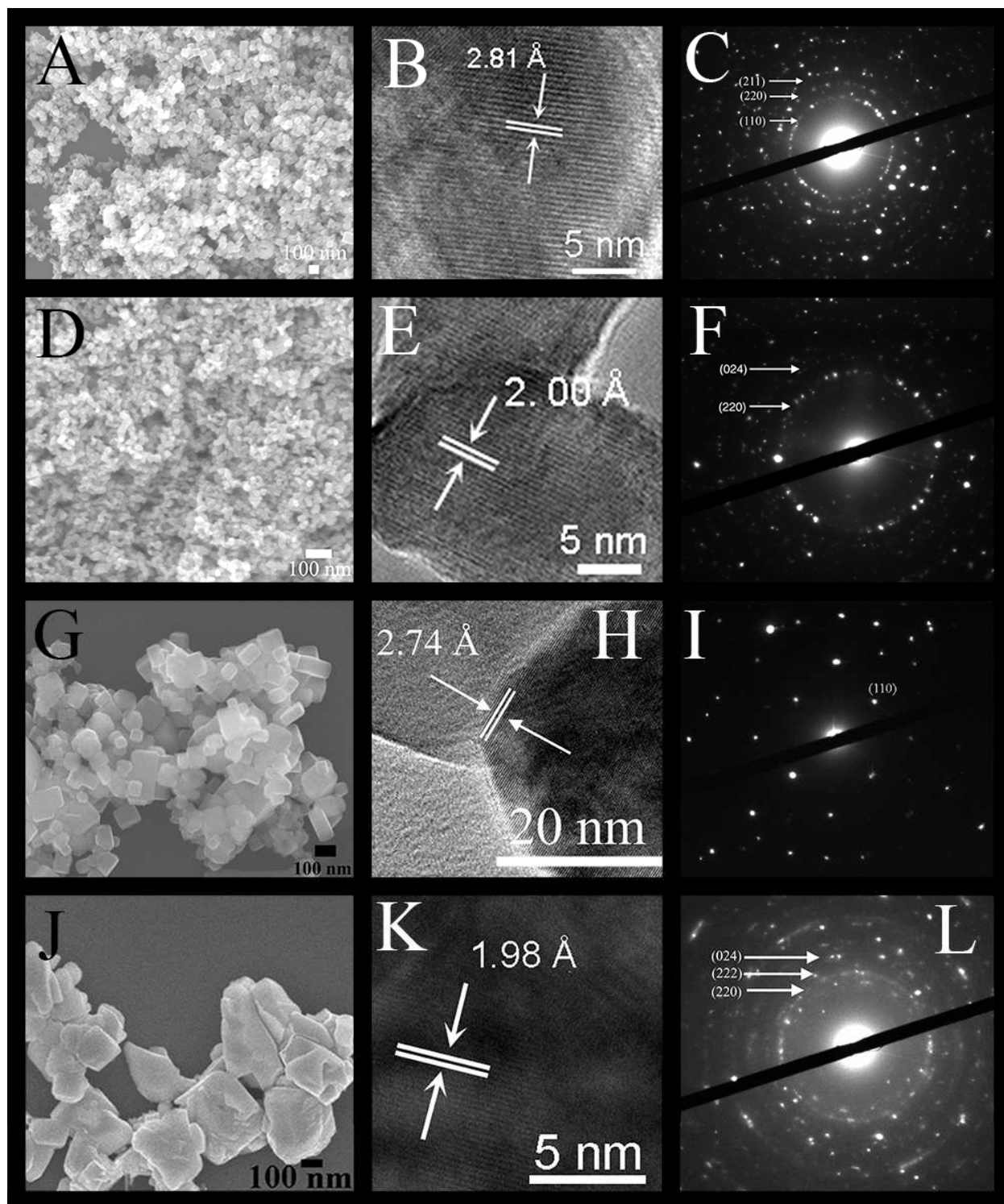
Figure 2.

Material	Nanoparticle Size (nm)	BET Surface Area (m^2/g)	Measured d-spacing (Å)	Metal Oxide Plane	Actual d-spacing (Å)
TiO$_2$	11.4 ± 2.8	129.32	3.57	(101)	3.51
RuO$_2$	35.0 ± 3	4.68	3.13	(110)	3.17
SrTiO$_3$	40.7 ± 0.7	29.02	2.81	(110)	2.76
SrRuO$_3$	37.3	54.49	2.00	(220)	1.96
SrTiO$_3$	113.0 ± 40	9.79	2.74	(110)	2.76
SrRuO$_3$	146.0 ± 49	11.43	1.98	(220)	1.96

Table 1.
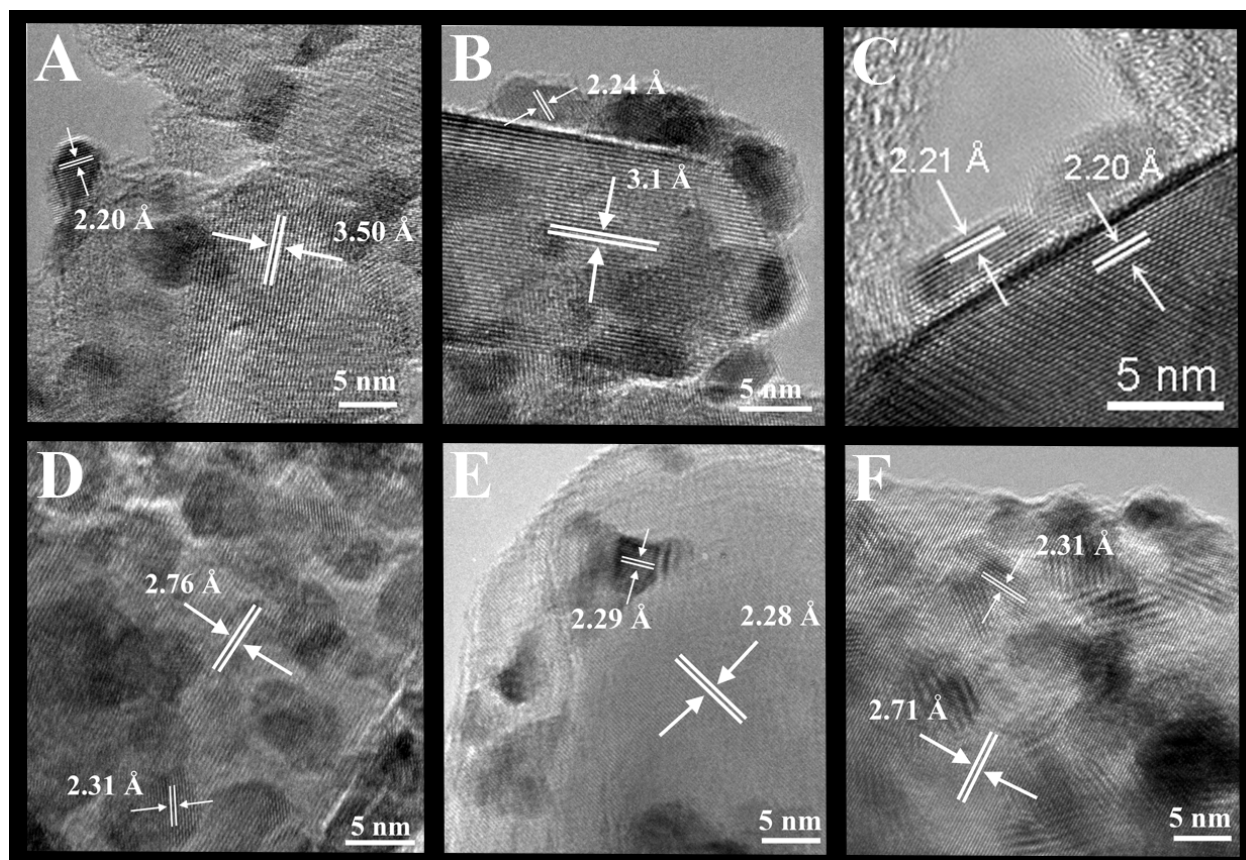
Figure 3.

Support Material	Measured *d*-spacing (Å)	Metal Oxide Plane	Measured Pt *d*-spacing (Å)	Pt Plane
TiO$_2$ (11.4 nm)	3.50	(101)	2.20	(111)
RuO$_2$ (35 nm)	3.10	(110)	2.24	(111)
SrTiO$_3$ (40.7 nm)	2.20	(200)	2.21	(111)
SrRuO$_3$ (37.3 nm)	2.76	(020)	2.31	(111)
SrTiO$_3$ (113 nm)	2.28	(111)	2.29	(111)
SrRuO$_3$ (146 nm)	2.71	(020)	2.31	(111)

Table 2.
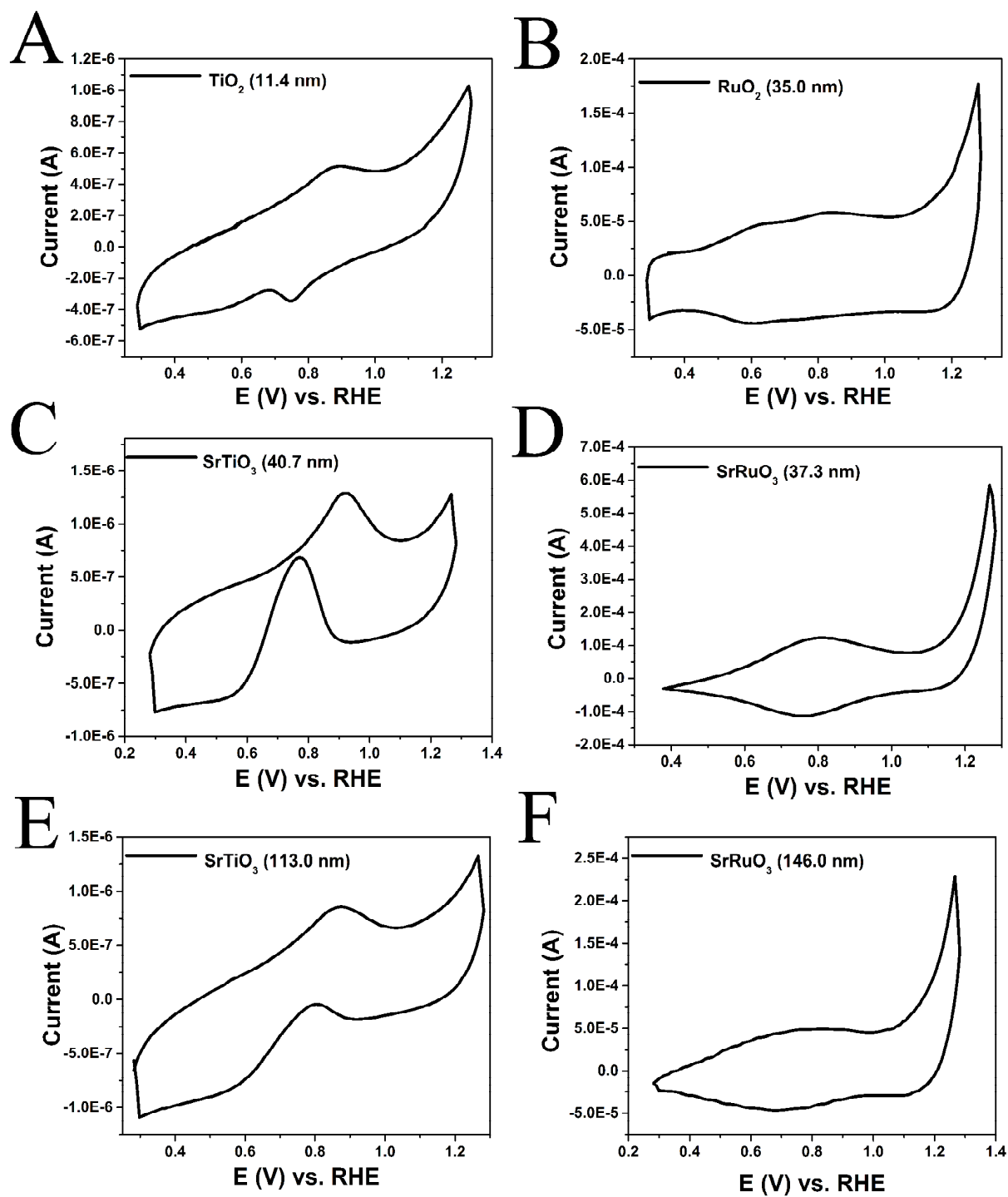
Figure 4.
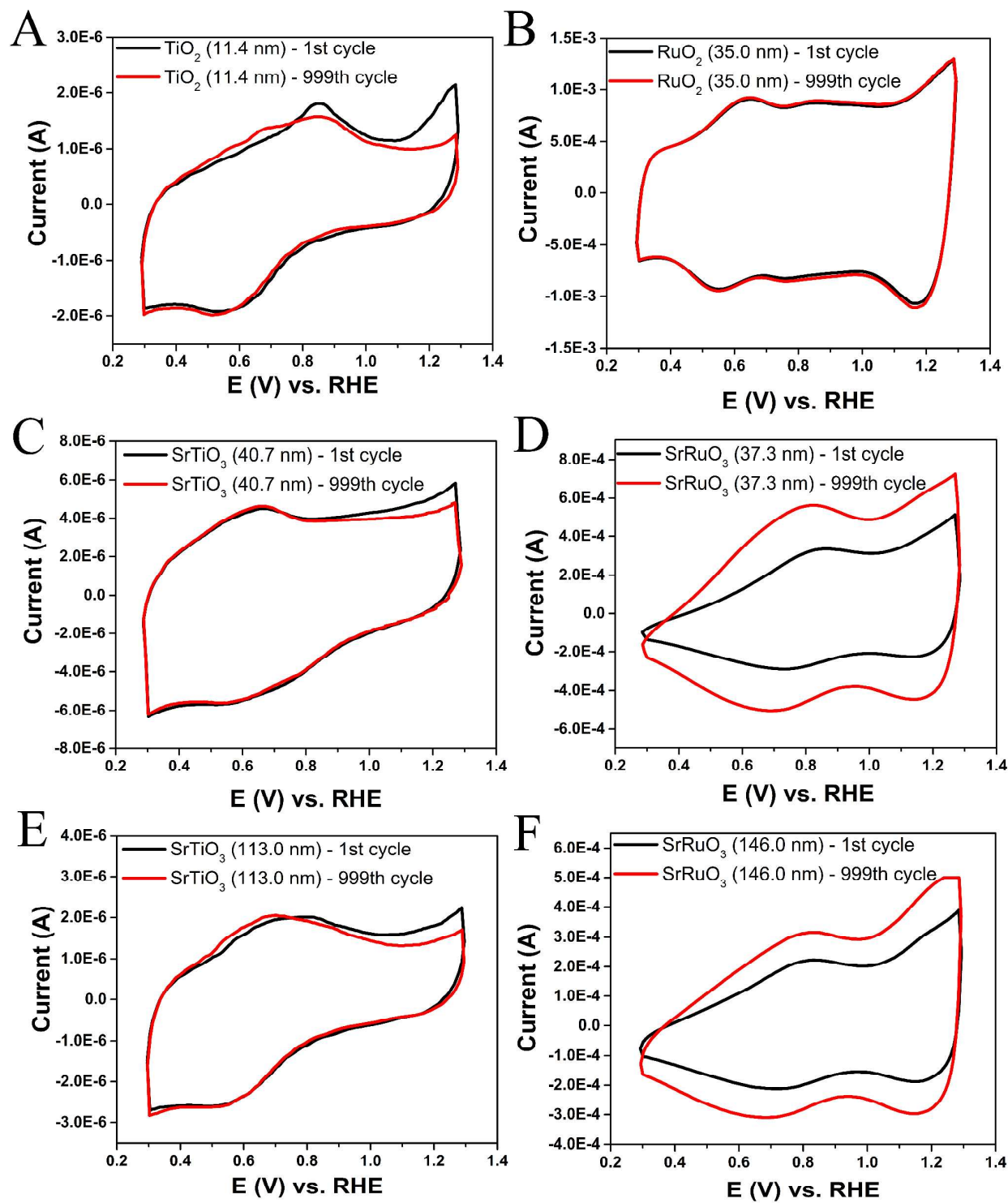
Figure 5.
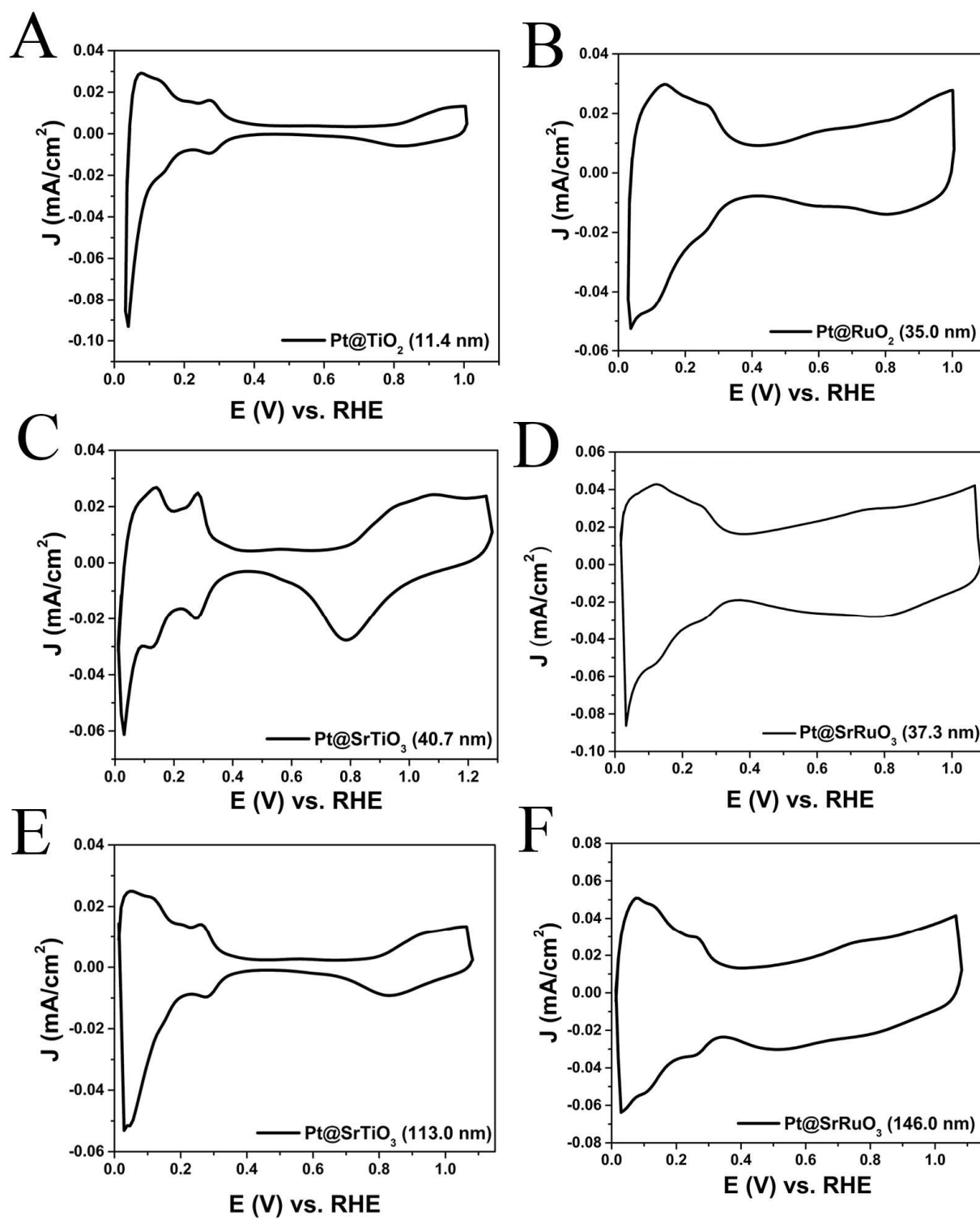
Figure 6.
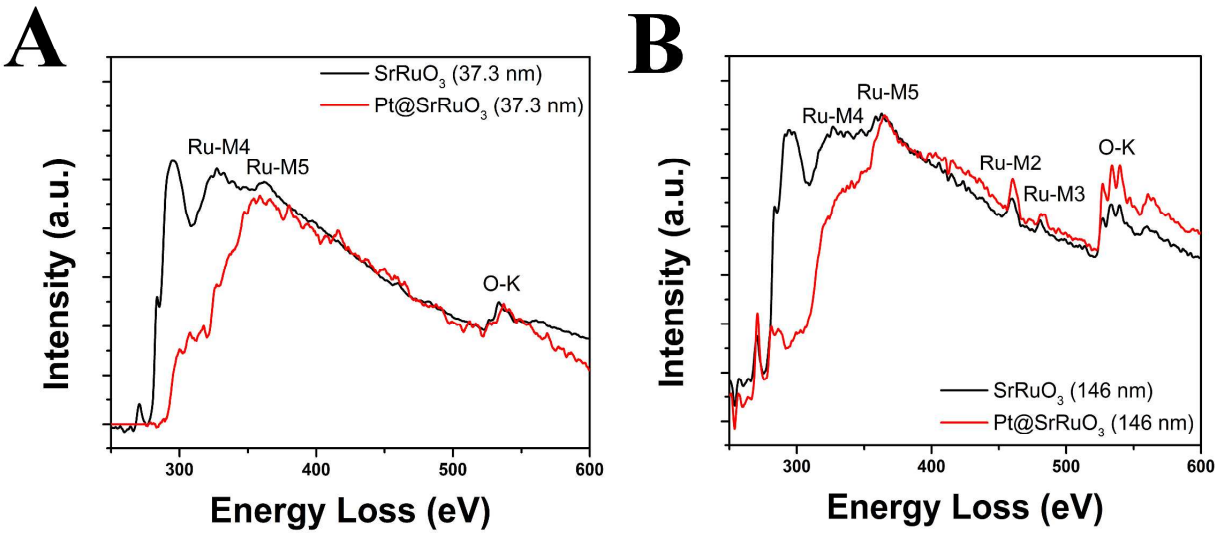
Figure 7.
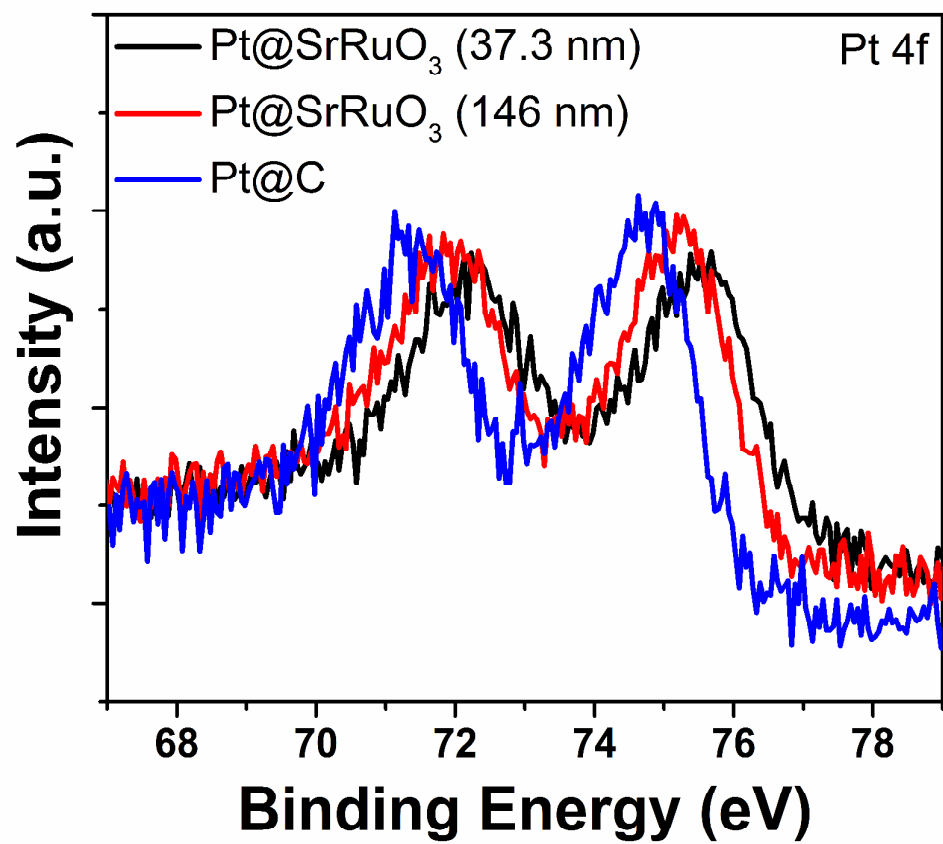
Figure 8.
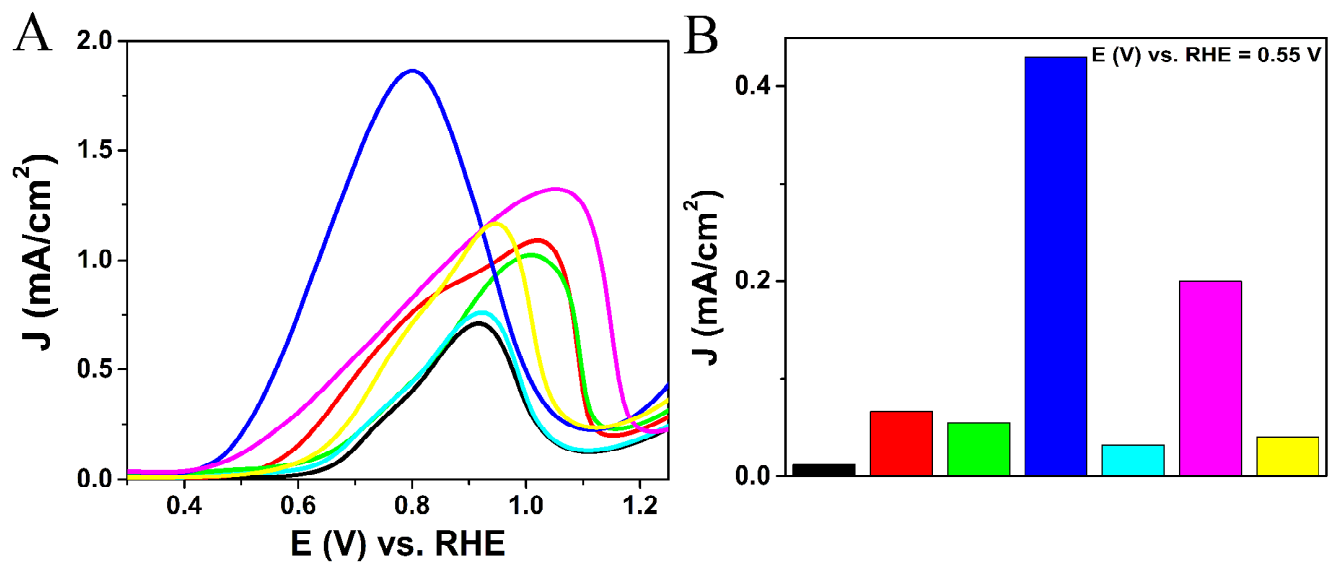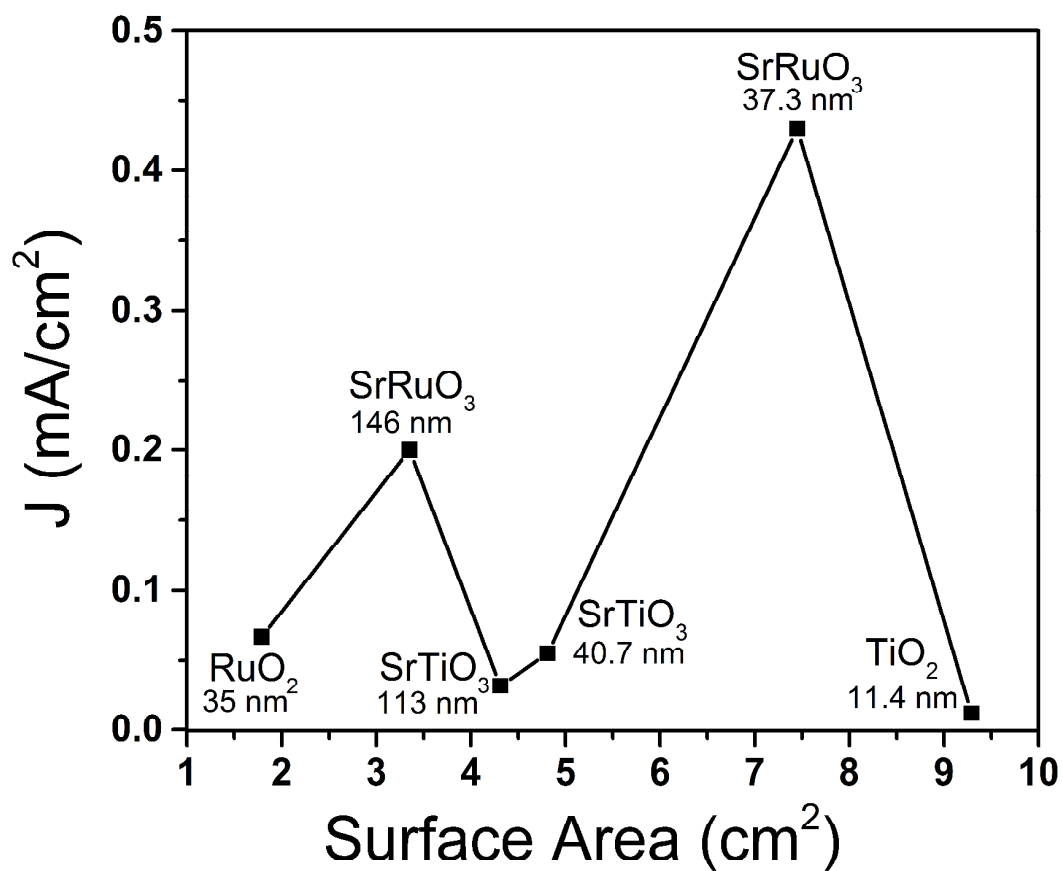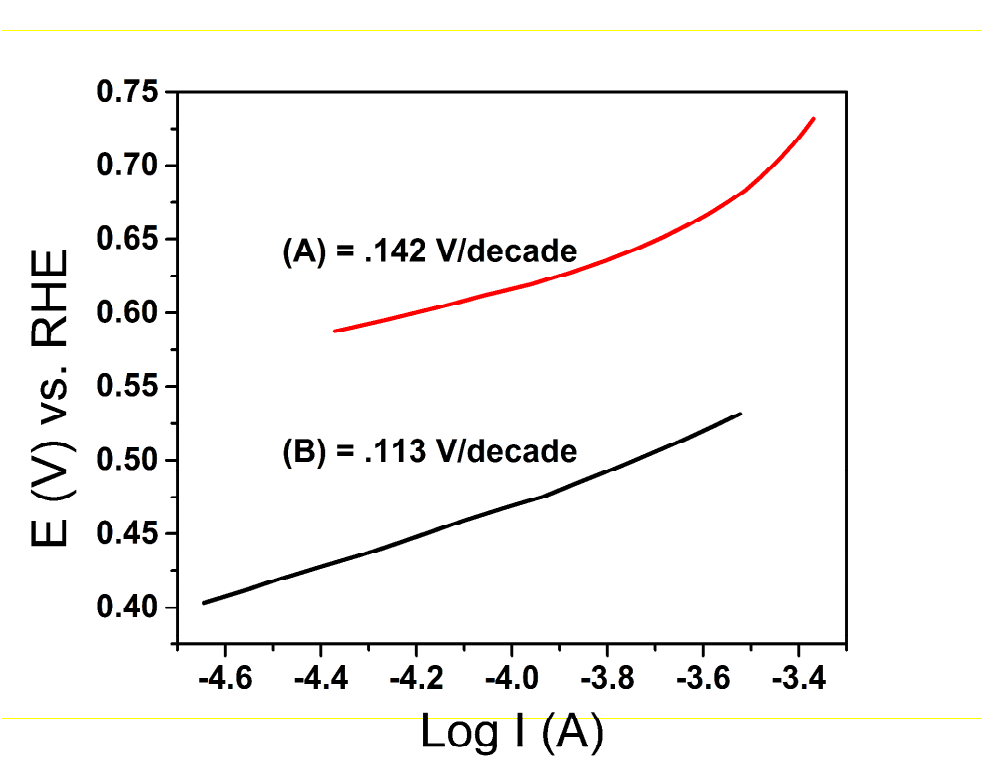
Figure 9.

Figure 10.

Figure 11.
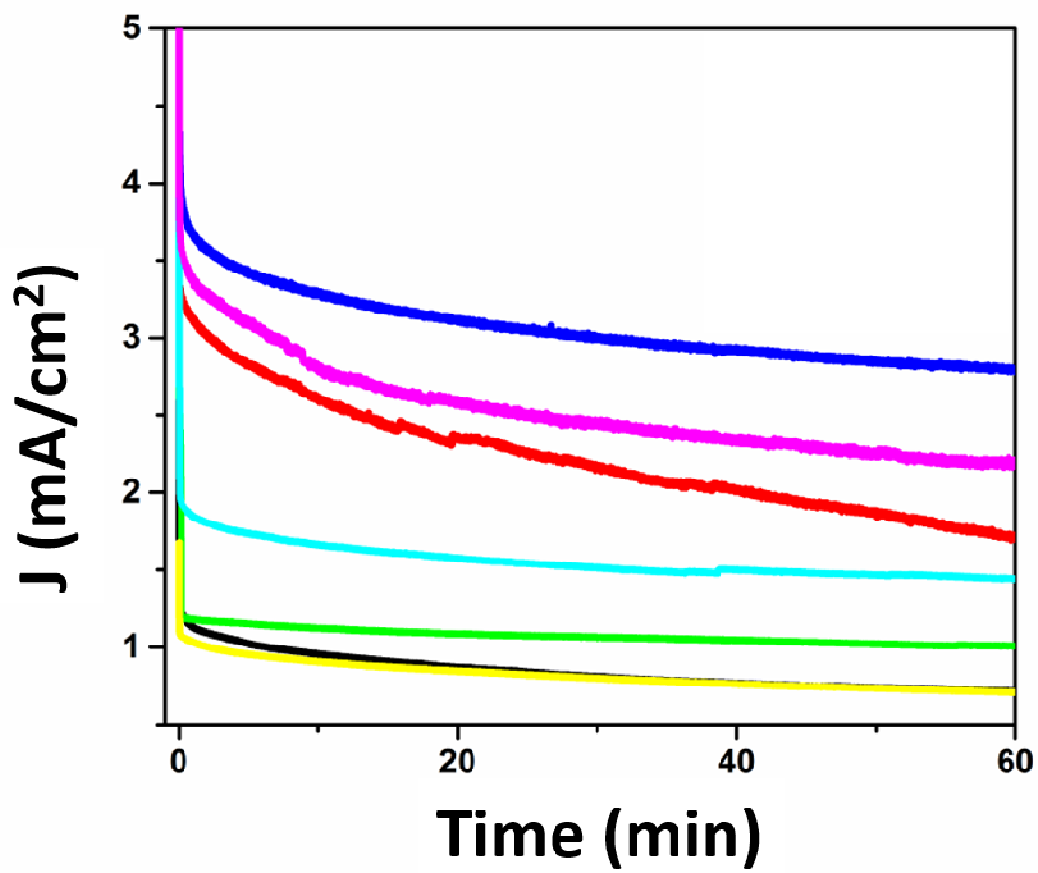
Figure 12.

| Material	J (mA/cm^2) E(V) vs. RHE = 0.7	Steady State Current Densities after 60 min (mA/cm^2 @ E(V) vs. RHE = 0.7)
Pt/TiO$_2$ (11.4 nm)	0.15	0.75
Pt/RuO$_2$ (35 nm)	0.48	1.7
Pt/SrTiO$_3$ (40.7 nm)	0.2	1.05
Pt/SrRuO$_3$ 37.3 nm)	1.42	2.8
Pt/SrTiO$_3$ (113 nm)	0.2	1.5
Pt/SrRuO$_3$ (146 nm)	0.57	2.2
Commercial Pt/C	0.31	0.7

Table 3.

References

1. P. J. Kulesza, I. S. Pieta, I. A. Rutkowska, A. Wadas, D. Marks, K. Klak, L. Stobinski and J. A. Cox, *Electrochimica Acta*, 2013, **110**, 474-483.
2. J. M. Campelo, D. Luna, R. Luque, J. M. Marinas and A. A. Romero, *ChemSusChem*, 2009, **2**, 18-45.
3. K. Lasch, G. Hayn, L. Jörissen, J. Garche and O. Besenhardt, *Journal of Power Sources*, 2002, **105**, 305-310.
4. H. Hua, C. Hu, Z. Zhao, H. Liu, X. Xie and Y. Xi, *Electrochimica Acta*, 2013, **105**, 130-136.
5. J. M. Macak, P. J. Barczuk, H. Tsuchiya, M. Z. Nowakowska, A. Ghicov, M. Chojak, S. Bauer, S. Virtanen, P. J. Kulesza and P. Schmuki, *Electrochemistry Communications*, 2005, **7**, 1417-1422.
6. M. Hepel, I. Kumarihamy and C. J. Zhong, *Electrochemistry Communications*, 2006, **8**, 1439-1444.
7. G. Zhao, L. Zhang, K. Sun and H. Li, *Journal of Power Sources*, 2014, **245**, 892-897.
8. L. Cao, F. Scheiba, C. Roth, F. Schweiger, C. Cremers, U. Stimming, H. Fuess, L. Chen, W. Zhu and X. Qiu, *Angewandte Chemie International Edition*, 2006, **45**, 5315-5319.
9. H. M. Villullas, F. I. Mattos-Costa and L. O. S. Bulhões, *The Journal of Physical Chemistry B*, 2004, **108**, 12898-12903.
10. A. L. Santos, D. Profeti and P. Olivi, *Electrochimica Acta*, 2005, **50**, 2615-2621.
11. V. A. Gercher, D. F. Cox and J.-M. Themlin, *Surface Science*, 1994, **306**, 279-293.
12. M. S. Saha, R. Li and X. Sun, *Electrochemistry Communications*, 2007, **9**, 2229-2234.
13. S. Penner and M. Armbrüster, *ChemCatChem*, 2015, **7**, 374-392.
14. A. Lan and A. S. Mukasyan, *Industrial & Engineering Chemistry Research*, 2008, **47**, 8989-8994.
15. S. Sharma and B. G. Pollet, *Journal of Power Sources*, 2012, **208**, 96-119.
16. E. Antolini and E. R. Gonzalez, *Solid State Ionics*, 2009, **180**, 746-763.
17. F. Shi, L. R. Baker, A. Hervier, G. A. Somorjai and K. Komvopoulos, *Nano Letters*, 2013, **13**, 4469-4474.
18. M. E. Scofield, H. Liu and S. S. Wong, *Chemical Society Reviews*, 2015, **44**, 5836-5860.
19. A. Lewera, L. Timperman, A. Roguska and N. Alonso-Vante, *The Journal of Physical Chemistry C*, 2011, **115**, 20153-20159.
20. L. Timperman, A. Lewera, W. Vogel and N. Alonso-Vante, *Electrochemistry Communications*, 2010, **12**, 1772-1775.
21. K. Hayek, R. Kramer and Z. Paál, *Applied Catalysis A: General*, 1997, **162**, 1-15.
22. A. Lan and A. S. Mukasyan, *The Journal of Physical Chemistry C*, 2007, **111**, 9573-9582.
23. A. L. Tiano, A. C. Santulli, C. Koenigsmann, M. Feygenson, M. C. Aronson, R. Harrington, J. B. Parise and S. S. Wong, *Chemistry of Materials*, 2011, **23**, 3277-3288.
24. J. H. White and A. F. Sammells, *Journal of The Electrochemical Society*, 1993, **140**, 2167-2177.
25. M. A. Peña and J. L. G. Fierro, *Chemical Reviews*, 2001, **101**, 1981-2018.
26. A. L. Sauvet, J. Fouletier, F. Gaillard and M. Primet, *Journal of Catalysis*, 2002, **209**, 25-34.
27. S. Ponce, M. A. Peña and J. L. G. Fierro, *Applied Catalysis B: Environmental*, 2000, **24**, 193-205.

28.   Y. Mao and S. S. Wong, *Journal of the American Chemical Society*, 2006, **128**, 8217-8226.

29.   J. Walker, R. Bruce King and R. Tannenbaum, *Journal of Solid State Chemistry*, 2007, **180**, 2290-2297.

30.   C. Chen, Q. Dai, C. Miao, L. Xu and H. Song, *RSC Advances*, 2015, **5**, 4844-4852.

31.   N. F. Atta, A. Galal and S. M. Ali, *International Journal of Electrochemical Science*, 2012, **7**, 725-746.

32.   Y. Mao, S. Banerjee and S. S. Wong, *Journal of the American Chemical Society*, 2003, **125**, 15718-15719.

33.   S. Mayavan, A. Mandalam, M. Balasubramanian, J.-B. Sim and S.-M. Choi, *Materials Research Bulletin*, 2015, **67**, 215-219.

34.   J.-D. Qiu, G.-C. Wang, R.-P. Liang, X.-H. Xia and H.-W. Yu, *The Journal of Physical Chemistry C*, 2011, **115**, 15639-15645.

35.   T. L. Duan, J. S. Pan and D. S. Ang, *ECS Journal of Solid State Science and Technology*, 2015, **4**, P364-P368.

36.   H. Wang, J. Lu, C. L. Marshall, J. W. Elam, J. T. Miller, H. Liu, J. A. Enterkin, R. M. Kennedy, P. C. Stair, K. R. Poeppelmeier and L. D. Marks, *Catalysis Today*, 2014, **237**, 71-79.

37.   B. Hasa, E. Kalamaras, E. I. Papaioannou, L. Sygellou and A. Katsaounis, *International Journal of Hydrogen Energy*, 2013, **38**, 15395-15404.

38.   A. C. Santulli, C. Koenigsmann, A. L. Tiano, D. DeRose and S. S. Wong, *Nanotechnology*, 2011, **22**, 1-13.

39.   W. Sugimoto, T. Kizaki, K. Yokoshima, Y. Murakami and Y. Takasu, *Electrochimica Acta*, 2004, **49**, 313-320.

40.   J. W. Long, K. E. Swider, C. I. Merzbacher and D. R. Rolison, *Langmuir*, 1999, **15**, 780-785.

41.   X. Guan and L. Guo, *ACS Catalysis*, 2014, **4**, 3020-3026.

42.   T. Xian and H. Yang, *Advanced Materials Research*, 2011, **418-420**, 18-21.

43.   M. Li, P. Liu and R. R. Adzic, *The Journal of Physical Chemistry Letters*, 2012, **3**, 3480-3485.

44.   T. Hepel, F. H. Pollak and W. E. O'Grady, *Journal of The Electrochemical Society*, 1984, **131**, 2094-2100.

45.   M. B. Vukmirovic, P. Liu, J. T. Muckerman and R. R. Adzic, *The Journal of Physical Chemistry C*, 2007, **111**, 15306-15311.

46.   H. Hua, C. Hu, Z. Zhao, H. Liu, X. Xie and Y. Xi, *Electrochimica Acta*, 2013, **105**, 130-136.

47.   S. V. Selvaganesh, G. Selvarani, P. Sridhar, S. Pitchumani and A. K. Shukla, *Journal of The Electrochemical Society*, 2012, **159**, B463-B470.

48.   J. G. Zhou, H. T. Fang, Y. F. Hu, T. K. Sham, C. X. Wu, M. Liu and F. Li, *The Journal of Physical Chemistry C*, 2009, **113**, 10747-10750.

49.   X. Liu, T. Pichler, M. Knupfer, J. Fink and H. Kataura, *Physical Review B*, 2004, **70**, 205405.

50.   A. Lewera, W. P. Zhou, R. Hunger, W. Jaegermann, A. Wieckowski, S. Yockel and P. S. Bagus, *Chemical Physics Letters*, 2007, **447**, 39-43.

51.   L. Liao, H. X. Mai, Q. Yuan, H. B. Lu, J. C. Li, C. Liu, C. H. Yan, Z. X. Shen and T. Yu, *The Journal of Physical Chemistry C*, 2008, **112**, 9061-9065.

52.   A. Bisht, P. Zhang, C. Shivakumara and S. Sharma, *The Journal of Physical Chemistry C*, 2015, **119**, 14126-14134.
53.   D. Briggs and M. P. Seah, *Auger and X-ray Photoelectron Spectroscopy*, Wiley, New York, 2 edn., 1990.
54.   M. Wakisaka, S. Mitsui, Y. Hirose, K. Kawashima, H. Uchida and M. Watanabe, *The Journal of Physical Chemistry B*, 2006, **110**, 23489-23496.
55.   S. Petrović, V. Rakić, D. M. Jovanović and A. T. Baričević, *Applied Catalysis B: Environmental*, 2006, **66**, 249-257.
56.   H. B. Suffredini, V. Tricoli, N. Vatistas and L. A. Avaca, *Journal of Power Sources*, 2006, **158**, 124-128.
57.   J. Masud, M. T. Alam, Z. Awaludin, M. S. El-Deab, T. Okajima and T. Ohsaka, *Journal of Power Sources*, 2012, **220**, 399-404.
58.   E. A. Franceschini, M. M. Bruno, F. J. Williams, F. A. Viva and H. R. Corti, *ACS Applied Materials & Interfaces*, 2013, **5**, 10437-10444.
59.   J. W. Guo, T. S. Zhao, J. Prabhuram, R. Chen and C. W. Wong, *Electrochimica Acta*, 2005, **51**, 754-763.
60.   A. Kabbabi, R. Faure, R. Durand, B. Beden, F. Hahn, J. M. Leger and C. Lamy, *Journal of Electroanalytical Chemistry*, 1998, **444**, 41-53.
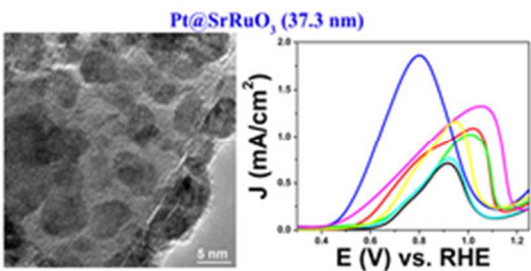
Explaining enhanced catalytic activity of Pt-supported metal oxide and perovskite substrates
22x11mm (300 x 300 DPI)